RSC Advances

REVIEW

View Article Online
View Journal | View Issue

Cite this: *RSC Adv.*, 2025, **15**, 42545

Bi_2MoO_6-based photocatalysts: engineering strategies for environmental and energy applications

Yiying Li, Zhilin Li, Enxiang Bi and Jingmei Li*

The rapid pace of economic and industrial development has led to increasingly severe environmental pollution and energy scarcity, emerging as pressing global concerns. Photocatalysis represents a promising strategy for addressing these dual challenges by converting solar energy into chemical energy or degrading pollutants. Among various photocatalysts, bismuth molybdate (Bi_2MoO_6), a representative Aurivillius-phase material, has garnered considerable attention owing to its visible-light-responsive bandgap, low toxicity, cost-effectiveness, and outstanding chemical stability. However, its practical application is significantly constrained by inherent drawbacks, including limited light absorption range and rapid recombination of photogenerated electron–hole pairs. This review presents a comprehensive overview of recent advances in Bi_2MoO_6-based photocatalysts, systematically examining synthesis methods, modification strategies (such as heterojunction construction, defect engineering, and elemental doping), and their diverse applications in both environmental remediation and energy conversion. Specifically, the environmental applications encompass the degradation of organic pollutants (*e.g.*, dyes and antibiotics), antibacterial activity, and performance in complex water matrices. In the energy sector, applications include photocatalytic hydrogen evolution, CO_2 reduction, and nitrogen fixation. Finally, the current challenges and future research directions for enhancing the photocatalytic performance of Bi_2MoO_6 are discussed, with the aim of guiding further investigation and facilitating its practical implementation in sustainable environmental and energy technologies.

Received 17th July 2025
Accepted 17th October 2025

DOI: 10.1039/d5ra05129k

rsc.li/rsc-advances

1. Introduction

The continuous development of industry and the economy has exacerbated environmental pollution. This pressing challenge poses a serious threat to the long-term sustainability of human civilization.[1] In response, many countries are intensifying research and development efforts aimed at advancing efficient and environmentally sustainable technologies. However, conventional environmental treatment technologies often suffer from several limitations, including low efficiency, the generation of harmful by-products, and difficulty in meeting increasingly stringent emission standards—particularly when addressing complex and variable pollution scenarios.[2] These challenges are even more pronounced in the treatment of organic contaminants and antibiotic residues, where the removal efficiency remains unsatisfactory.[3]

To alleviate environmental pressure and mitigate the adverse effects of pollutants on human health, the development of more efficient environmental purification and energy conversion technologies has become an urgent priority. Among various approaches, photocatalytic technology stands out due to its distinctive advantages. Utilizing renewable light energy, photocatalysts facilitate the conversion of toxic organic contaminants into harmless carbon dioxide and water, as well as the production of clean energy sources such as hydrogen and ammonia through processes like water splitting and nitrogen fixation.[4–6] In addition, photocatalytic technology has demonstrated varying degrees of effectiveness in treating a range of pollutants, including dinitrophenol,[7] phenol,[8–11] methyl orange,[12–14] bisphenol A(BPA),[15–17] trichlorophenol[18] *etc.* Compared to other treatment methods, photocatalytic technology offers advantages such as low energy consumption, cost-effectiveness, and the recyclability of photocatalysts, thereby providing significant environmental benefits.[19] It has demonstrated broad application potential across various fields, including renewable energy development, photocatalytic nitrogen fixation, pollutant degradation, and bacterial inhibition, making it a focal point of current research.

Among the various photocatalysts, traditional materials such as TiO_2 and g-C_3N_4 have been widely investigated. TiO_2, for instance, is renowned for its strong oxidation capability, stability, and low cost, but its wide bandgap (~3.2 eV) restricts its light absorption primarily to the ultraviolet region, which constitutes only a small fraction of solar energy.[20–23] g-C_3N_4, with a narrower bandgap (~2.7 eV), exhibits visible-light

School of Life Science and Technology, Changchun University of Science and Technology, Changchun, 130022, China. E-mail: ljm3023@126.com

activity; however, it often suffers from rapid charge recombination and limited surface area, constraining its overall efficiency.[24–26] In contrast, bismuth molybdate (Bi_2MoO_6), an emerging visible-light-responsive photocatalyst, has attracted considerable attention in photocatalysis due to its unique Aurivillius-layer structure, suitable band gap (2.5–2.8 eV) enabling enhanced visible-light harvesting compared to TiO_2, low toxicity, excellent stability, and cost-effectiveness.[27,28]

However, Bi_2MoO_6 still faces bottleneck problems such as fast photogenerated carrier recombination rate, limited light absorption capacity, and slow surface reaction kinetics, which limit the full play of its photocatalytic performance in practical applications. To overcome these limitations, the construction of Bi_2MoO_6-based composites has emerged as a central research focus. Extensive research has been dedicated to various modification strategies, including morphological control, ion doping, metal deposition, and—most prominently—heterojunction construction.[29] These modification techniques not only enhance the photocatalytic performance of Bi_2MoO_6 but also improve its stability and selectivity, thereby facilitating efficient pollutant degradation, antibacterial applications, and energy conversion processes such as hydrogen evolution and CO_2 reduction.

This review provides a comprehensive overview of the latest advances in Bi_2MoO_6-based photocatalysts, systematically examining their synthesis methods, modification strategies, and multifaceted applications. It delves into their roles in degrading environmental contaminants such as dyes and antibiotics, as well as their emerging applications in antibacterial treatments and energy conversion systems—including photocatalytic hydrogen evolution, CO_2 reduction, and nitrogen fixation. Furthermore, the review outlines future development trends and the associated challenges in the field. It is anticipated that this work will offer valuable insights and guidance for the rational design of efficient, stable, and eco-friendly Bi_2MoO_6 photocatalytic systems for both environmental and energy-related applications.

2. Methods for preparing Bi_2MoO_6-based photocatalytic materials

2.1. Hydrothermal method

The hydrothermal method stands as a pivotal and versatile synthesis technique in the design of advanced semiconductor photocatalysts. This liquid-phase process, which facilitates the dissolution and recrystallization of precursors within a sealed vessel under autogenous pressure, is particularly valued for enabling precise control over critical material characteristics. These include the morphology, size, and specific surface area of the resulting nanomaterials, all of which are fundamental determinants of photocatalytic performance. Hydrothermal synthesis methods have been widely employed in the preparation of semiconductor photocatalysts owing to their simplicity, low cost, and capacity to produce nanostructured materials with relatively uniform morphology. In particular, numerous Bi_2MoO_6-based photocatalysts have been successfully synthesized *via* hydrothermal routes, such as Ag/AgBr/Bi_2MoO_6,[30] g-C_3N_4/Bi_2MoO_6,[31] Bi/Bi_2MoO_6,[32] BiOCOOH/Bi_2MoO_6,[33] and $Bi_{19}Cl_3S_{27}$/Bi_2MoO_6.[34] This capability is further enhanced by the strategic use of surfactants and structure-directing agents. For instance, employing surfactants such as sodium dodecyl sulfate, polyvinylpyrrolidone, and cetyltrimethylammonium bromide allows for the synthesis of Bi_2MoO_6 single crystals with precisely controlled size and morphology.[35–38] Among these, Bi_2MoO_6 synthesized with cetyltrimethylammonium bromide exhibited superior photocatalytic activity under simulated sunlight, degrading 98% of methylene blue (MB) within 90 minutes. This enhanced performance is attributed to its ultra-fine nanocrystal structure and high specific surface area.[39]

In addition, composites of Bi_2MoO_6 and banana peel-derived biochar (BPB) were synthesized *via* a hydrothermal method (Fig. 1a). Visible-light-driven ciprofloxacin (CIP) degradation tests conducted in artificial seawater demonstrated that incorporating BPB into Bi_2MoO_6 significantly enhances photocatalytic efficiency. The BPB/Bi_2MoO_6 (1 : 4) composite exhibits a rate constant of 0.0486 min^{-1}, approximately 12.5 times higher than that of pure Bi_2MoO_6 (0.0039 min^{-1}), underscoring the effectiveness of BPB in enhancing reaction kinetics. As shown in the photoluminescence (PL) spectra (Fig. 1b), the incorporation of BPB leads to a marked reduction in the emission peak at ~470 nm, indicating suppressed electron–hole recombination and improved charge separation within the composite. Furthermore, the photocurrent response illustrated in Fig. 1c reveals that the BPB/Bi_2MoO_6 (1 : 4) composite exhibits superior charge transport efficiency compared to pure Bi_2MoO_6. This enhancement is attributed to the strong interfacial coupling between Bi_2MoO_6 and BPB, which facilitates efficient charge migration. Electrochemical impedance spectroscopy (EIS) measurements (Fig. 1d) further confirm improved charge separation at the heterojunction interface, as indicated by the smaller arc radius in the Nyquist plot, reflecting lower charge transfer resistance. The optimized interface effectively suppresses charge recombination, thereby increasing the availability of free carriers for photocatalytic reactions. Consequently, the synergistic interaction between Bi_2MoO_6 and BPB enhances photocatalytic performance by promoting charge transfer and minimizing recombination losses.[40]

Furthermore, Huang *et al.* successfully synthesized a novel $BiIO_4$/Bi_2MoO_6 heterojunction photocatalyst *via* a one-step hydrothermal method. Compared to pure $BiIO_4$ and Bi_2MoO_6, the composite exhibited significantly enhanced visible-light photocatalytic activity for the degradation of rhodamine B (RhB).[41]

Notwithstanding its extensive utility, the hydrothermal method is not without inherent limitations that can impact reproducibility and scalability. Common challenges associated with the technique include non-uniform temperature distribution within the reaction vessel, significant solution temperature gradients, and relatively slow heating rates, all of which can impede the precise control of crystal growth and final morphology. Furthermore, the typically lengthy reaction times and the inability to perform *in situ* monitoring of the

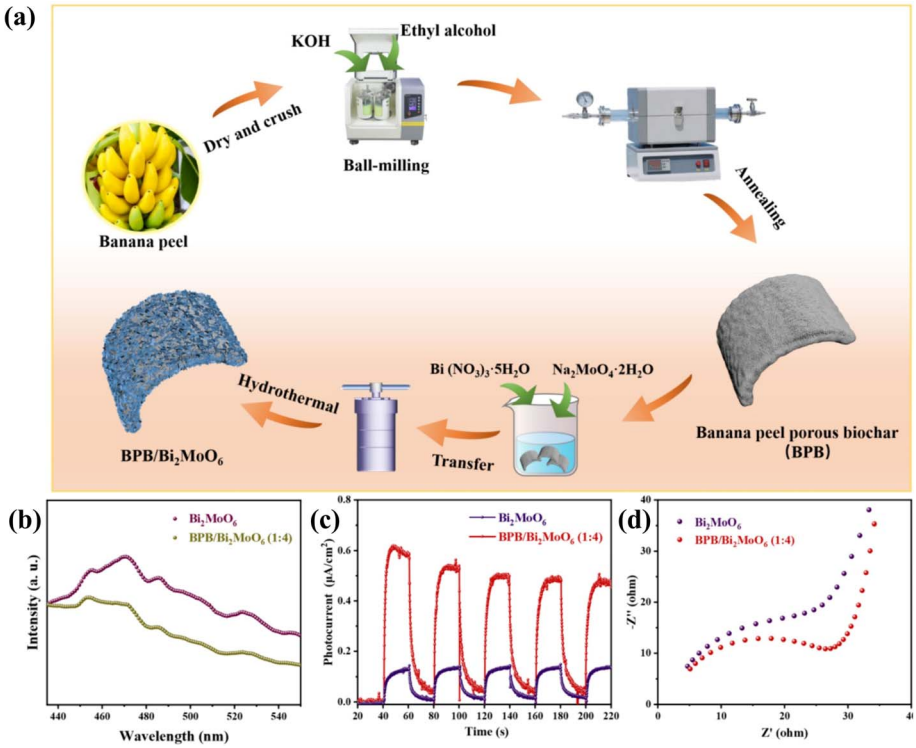

Fig. 1 (a) Process flow chart of synthesizing BPB/Bi_2MoO_6 composite. (b) PL spectra, (c) photocurrent responses, and (d) EIS analysis of Bi_2MoO_6 and BPB/Bi_2MoO_6 (1 : 4). Reproduced from ref. 40 with permission from Elsevier. Copyright 2024.

crystallization process pose significant constraints on the efficient optimization of reaction parameters. Despite these challenges, ongoing methodological refinements and the strategic design of composite materials continue to make hydrothermal synthesis a highly productive route for developing high-performance photocatalysts.

2.2. Solvothermal method

The solvothermal method represents a significant extension of the hydrothermal technique, wherein non-aqueous solvents are employed as the reaction medium. This key modification profoundly expands the synthetic toolbox for advanced photocatalysts by leveraging adjustable solvent properties such as polarity, boiling point, and coordination ability. These parameters provide enhanced control over nucleation and crystal growth, enabling the precise fabrication of nanomaterials with diverse and complex architectures, which are often unattainable through purely aqueous routes. A common theme across numerous studies is the critical influence of reaction conditions, particularly temperature and solvent composition, on the final product's morphology and, consequently, its photocatalytic performance.[42,43]

The Bi_2MoO_6/N-rGO composite, synthesized *via* a solvothermal method, exhibits enhanced photocatalytic activity (Fig. 2g). HRSEM images reveal clear morphological differences among the samples: pristine Bi_2MoO_6 consists of aggregated nanorods approximately 2 μm in length (Fig. 2a and b), while rGO incorporation promotes the formation of nanoplates (Fig. 2c). N-doping (Fig. 2d) maintains a similar morphology to the undoped composite. The PL spectra provide insights into carrier recombination behavior; lower PL intensity indicates improved charge separation. As shown in Fig. 2e, the Bi_2MoO_6/N-rGO composite exhibits the weakest PL signal, suggesting significantly suppressed electron–hole recombination and thus enhanced photocatalytic efficiency. EIS results (Fig. 2f) show that this composite has the smallest semicircle in the Nyquist plot, indicating the lowest charge transfer resistance among the samples. The formation of a heterojunction between Bi_2MoO_6 and N-rGO facilitates efficient electron migration from the conduction band (CB) of Bi_2MoO_6 to the N-rGO sheets. Owing to the unique electronic properties of graphene, N-rGO can effectively accept and transport electrons, thereby promoting interfacial redox reactions with surrounding pollutant molecules.[44]

Chankhanittha *et al.* synthesized an efficient Bi_2MoO_6 photocatalyst at low temperatures using a solvothermal method. The orthorhombic Bi_2MoO_6 catalyst achieved up to 90% photodegradation efficiency against two azo dyes (Reactive Red and Congo Red) and two antibiotics (ofloxacin and norfloxacin) under both UV and visible light irradiation.[45] Zhang and his team synthesized Bi_2MoO_6/ZnO photocatalysts with well-defined interfacial contact using a solvothermal method. By adjusting the precursor concentration, they obtained two Bi_2MoO_6/ZnO composites with distinct morphologies—nanoparticles and nanosheets. Under visible light irradiation, the Bi_2MoO_6/ZnO composites exhibited significantly higher photoreduction activity toward Cr(VI) compared to pure Bi_2MoO_6 and

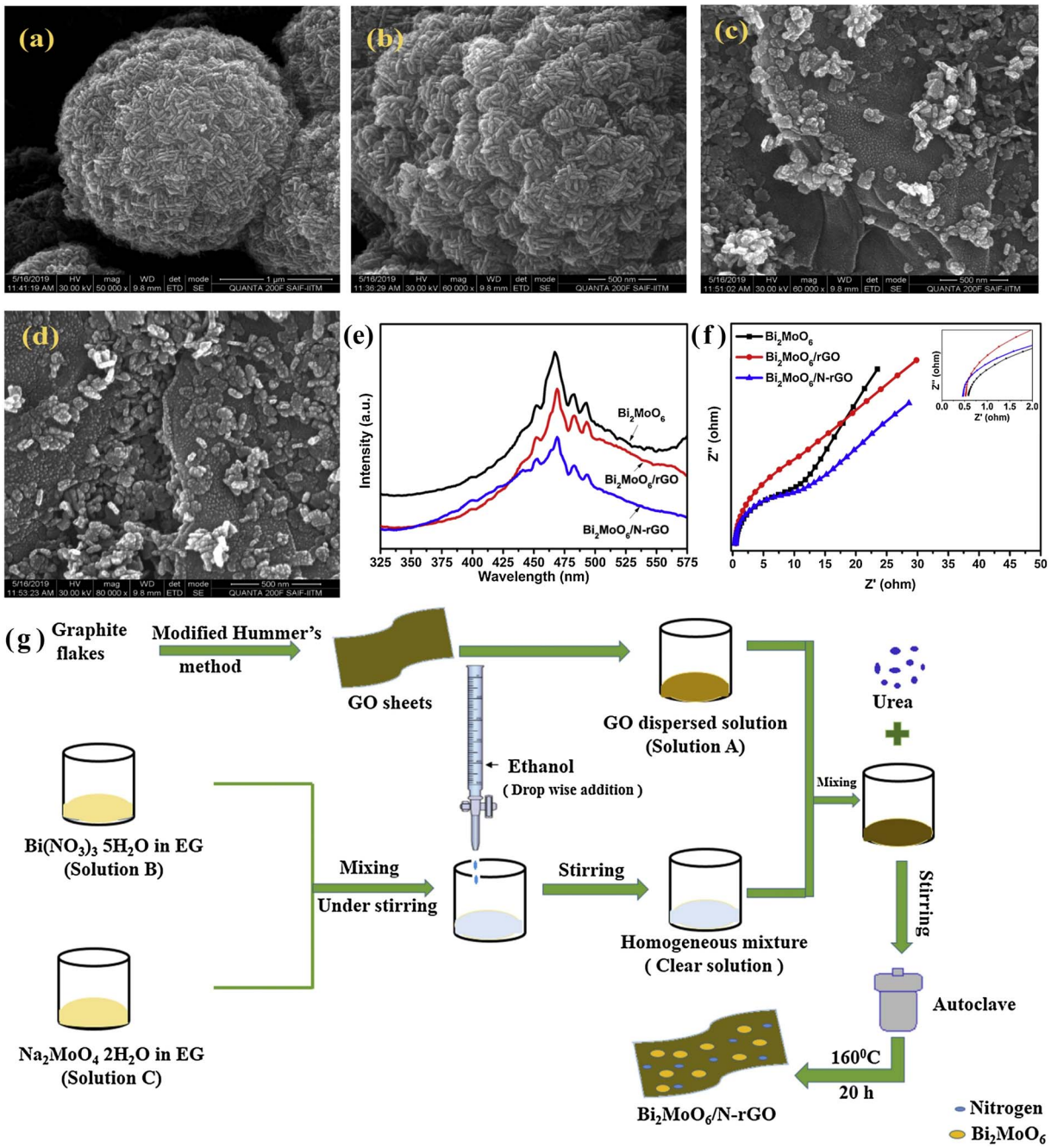

Fig. 2 (a and b) HR-SEM images of bare Bi_2MoO_6, (c) Bi_2MoO_6/rGO, (d) Bi_2MoO_6/N-rGO; (e) PL spectra and (f) electrochemical impedance spectra of bare Bi_2MoO_6, Bi_2MoO_6/rGO and Bi_2MoO_6/N-rGO catalysts. (g) Schematic diagram of the synthesis of Bi_2MoO_6/N-rGO composite catalyst. Reproduced from ref. 44 with permission from Elsevier. Copyright 2024.

ZnO. The composite also demonstrated a stronger photocurrent response and lower electrochemical impedance than its individual components, indicating more efficient separation and transfer of photogenerated charge carriers. The formation of a layered heterojunction between Bi_2MoO_6 and ZnO contributes to the enhanced charge separation efficiency and overall photocatalytic performance. Moreover, the Bi_2MoO_6/ZnO photocatalyst maintained excellent stability over three consecutive photocatalytic cycles.[46] Zhang *et al.* synthesized Bi_2MoO_6/$Bi_2Sn_2O_7$ composite photocatalytic materials using a solvothermal method to create a three-dimensional layered structure. It was discovered that the ability to photodegradation ability substances using light of Bi_2MoO_6/$Bi_2Sn_2O_7$. The composite for RhB and tetracycline (TC) under LED irradiation was much higher than that of unadulterated Bi_2MoO_6 and pure $Bi_2Sn_2O_7$.[47]

Compared with the hydrothermal method, the solvothermal method, which utilizes organic or non-aqueous solvents,

provides enhanced control over the reaction environment through adjustable parameters such as solvent polarity, boiling point, and coordination behavior. This facilitates better tuning of nucleation and growth processes, offering greater structural and morphological diversity in the resulting photocatalysts. Additionally, solvothermal systems often allow lower reaction temperatures and shorter synthesis times, and are more adaptable to the incorporation of organic–inorganic interfaces and hybrid nanostructures. However, limitations such as potential toxicity or flammability of organic solvents, higher cost, and complexity in post-processing and purification may hinder large-scale application.

2.3. Electrospinning method

Electrospinning has been strategically employed to engineer Bi_2MoO_6-based photocatalysts into unique one-dimensional and hierarchical nanostructures—such as fibers, tubes, and belts—which are pivotal for overcoming charge recombination and mass transfer limitations. This technique utilizes a high-voltage electrostatic field to draw a charged polymer solution into fine jets that solidify into continuous nanostructures, often using polymer templates as sacrificial frameworks to create bespoke morphologies difficult to achieve by other means.[48] In the context of Bi_2MoO_6, electrospinning excels in constructing materials with high specific surface area for abundant reactive sites, directional electron transport pathways that enhance charge separation, and self-supporting macroscopic structures that facilitate catalyst recovery and reuse. These collective attributes offer unparalleled advantages for enhancing the photocatalytic efficiency and practicality of Bi_2MoO_6 in environmental pollutant degradation.

One-dimensional Bi_2MoO_6 nanotubes were synthesized by Zhao *et al.* using electrospinning followed by a calcination process. Among the samples, the Bi_2MoO_6 nanotubes calcined at 600 °C for 2 hours exhibited superior photocatalytic activity under simulated sunlight compared to those treated at 500 °C or 700 °C, corresponding to γ-Bi_2MoO_6 phases.[49] Li *et al.* synthesized one-dimensional CeO_2/Bi_2MoO_6 nanofibers sensitized with 2,9,16,23-tetranitrocopper phthalocyanine (TNCuPc) *via* a combined electrospinning–solvothermal method, as illustrated in Fig. 3a. During the synthesis, TNCuPc particles were uniformly deposited *in situ* onto the surface of the CeO_2/Bi_2MoO_6 nanofibers. The resulting one-dimensional TNCuPc/CeO_2/Bi_2MoO_6 photocatalyst exhibited efficient photogenerated charge separation, a broad light absorption range, excellent photocatalytic performance toward TC under simulated sunlight, as well as good recyclability and long-term operational stability.[50] In the study by Zhang *et al.*, electrospun ternary composites composed of polyacrylonitrile (PAN), Bi_2MoO_6, and Ti_3C_2 (PAN/Bi_2MoO_6/Ti_3C_2) exhibited a 3.2-fold enhancement in TC photodegradation efficiency compared to pristine Bi_2MoO_6. The formation of a Bi_2MoO_6/Ti_3C_2 heterojunction effectively facilitated interfacial charge separation and inhibited charge carrier recombination. Meanwhile, the PAN matrix imparted mechanical integrity, enabling easy recovery and reuse of the photocatalyst film.[51] Xu *et al.* prepared a $Bi_2MoO_6/LaFeO_3$ heterojunction photocatalyst by combining electrospinning with solvothermal synthesis (Fig. 3b and c). By adjusting the concentrations of $Bi(NO_3)_3\cdot 5H_2O$ and $Na_2MoO_4\cdot 2H_2O$, the density and thickness of 2D n-type Bi_2MoO_6 nanosheets on 1D p-type $LaFeO_3$ hollow nanofibers were effectively controlled. The optimized $Bi_2MoO_6/LaFeO_3$-4 sample demonstrated superior visible-light photocatalytic degradation of tetracycline TC (92.31% in 30 minutes) with the highest rate constant (0.05526 min^{-1}). The possible mechanism for charge separation and migration during the tetracycline hydrochloride (TCH) photocatalytic degradation process using $Bi_2MoO_6/LaFeO_3$-4 is shown in Fig. 3d. Enhanced performance is attributed to the wide spectral response, direct Z-scheme p–n heterojunction, large surface area resulting from the 2D/1D architecture, rapid charge transfer, and a built-in electric field.[52]

Despite its morphological advantages, electrospinning suffers from several inherent drawbacks, including high operational costs, low production throughput, sensitivity to environmental conditions (*e.g.*, humidity, solvent volatility), and limited scalability, which significantly constrain its widespread industrial application. Consequently, its use remains less prevalent compared to more conventional techniques such as hydrothermal or solvothermal synthesis. Nevertheless, recent studies have demonstrated the successful preparation of high-performance Bi_2MoO_6-based composite photocatalysts *via* electrospinning, such as ZnO/γ-Bi_2MoO_6 heterostructure nanotubes,[53] one-dimensional SiO_2-doped Bi_2MoO_6 microstrips,[54] and $Bi_2MoO_6/ZnFe_2O_4$ heterostructure nanofibers[55] were prepared by electrospinning. All of them showed enhanced photocatalytic activity. These nanostructures exhibit significantly improved photocatalytic activity under visible light irradiation, attributed to enhanced charge separation, one-dimensional electron transport pathways, and increased reactive surface area.

2.4. Co-precipitation method

The co-precipitation method is a widely used wet-chemical technique for the synthesis of metal oxide photocatalysts due to its operational simplicity, low energy consumption, and ability to produce homogeneous multicomponent systems. A key advantage of this method is the achievement of molecular-level mixing of precursors, which promotes the formation of uniform phases and solid solutions, and is particularly conducive to constructing intimate heterojunction interfaces. In the context of Bi_2MoO_6-based photocatalysts, this method typically involves the simultaneous precipitation of bismuth and molybdate precursors in an aqueous medium under controlled pH and temperature conditions, followed by filtration, drying, and calcination. For instance, Yu *et al.* prepared ZnCuAl layered double hydroxide (LDH)/Bi_2MoO_6 nanocomposites *via* a steady-state co-precipitation strategy. The stacked LDH and Bi_2MoO_6 nanosheets provided abundant active sites, increasing the specific surface area of the composite to 19.1 $m^2\ g^{-1}$. Moreover, the formation of heterojunctions and potential quantum size effects extended the light absorption range of the LDH/Bi_2MoO_6 composites beyond that of pristine LDH and Bi_2MoO_6. Jin *et al.*

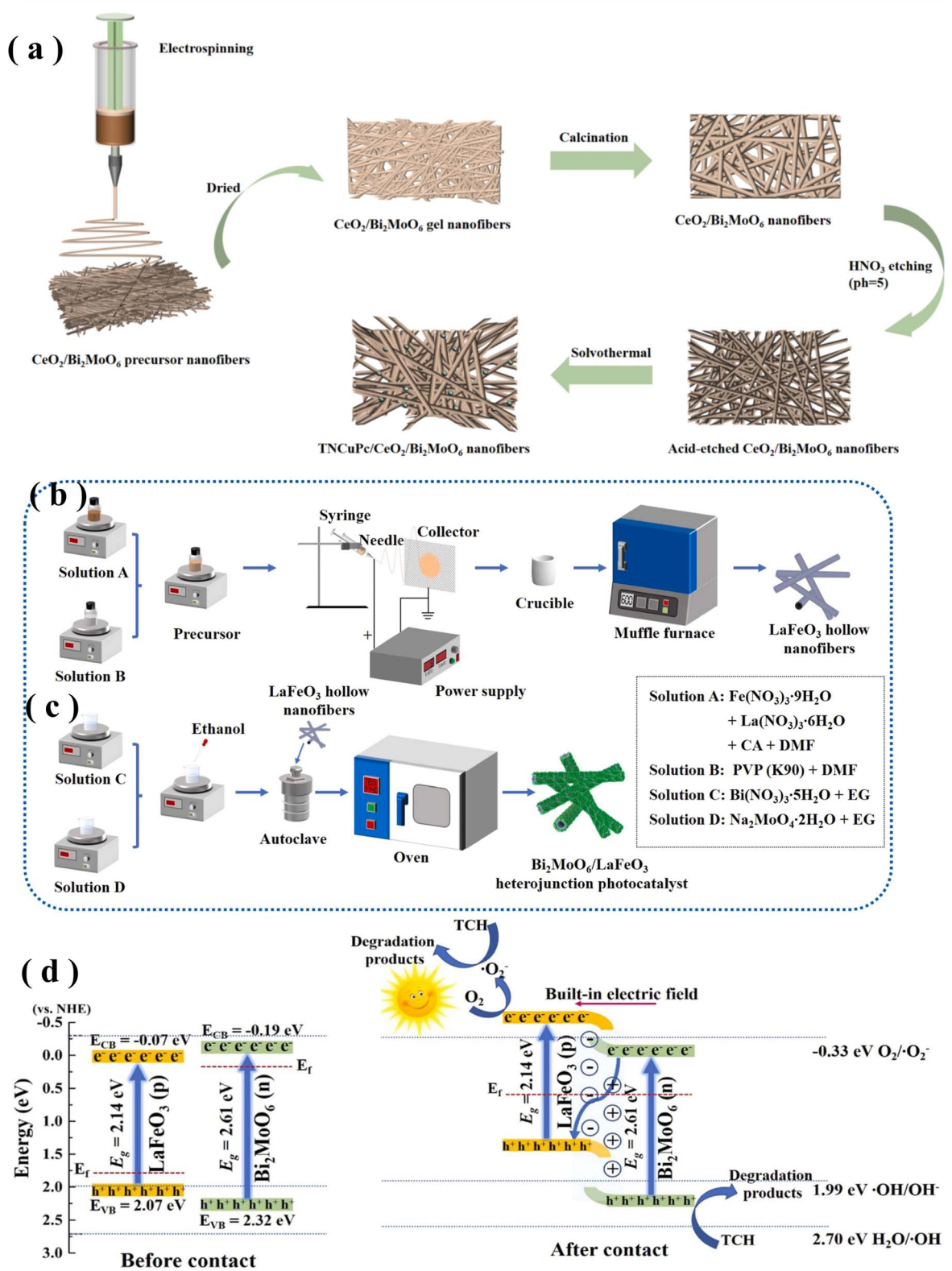

Fig. 3 (a) Schematic diagram of the experimental synthesis of TNCUPC/CeO_2/Bi_2MoO_6 nanofibers. (b) Illustration of the preparation of $LaFeO_3$ hollow nanofiber and (c) Bi_2MoO_6/$LaFeO_3$ heterojunction photocatalyst. (d) Illustration of possible mechanisms for charges separation and migration during photocatalytic degradation of TCH over Bi_2MoO_6/$LaFeO_3$-4. Reproduced from ref. 52 with permission from Elsevier. Copyright 2024.

synthesized a Ho^{3+}/Yb^{3+} co-doped Bi_2MoO_6 (Ho^{3+}/Yb^{3+}-Bi_2MoO_6) photocatalyst *via* co-precipitation followed by annealing. The resulting powder exhibited a spherical and flaky morphology and demonstrated significantly enhanced photocatalytic activity for RhB degradation compared to pristine Bi_2MoO_6.[56] Benazir *et al.* synthesized Bi_2MoO_6/MoS_2 nanocomposite using the co-precipitation method (Fig. 4a). The composite demonstrated high photocatalytic efficiency under UV light, degrading Rose Bengal and Acid Blue dyes by approximately 83% and 82% within 60 minutes, with stable activity over five cycles (Fig. 4b and c). MoS_2 synthesis involved dissolving precursors in water, mixing under stirring, adjusting

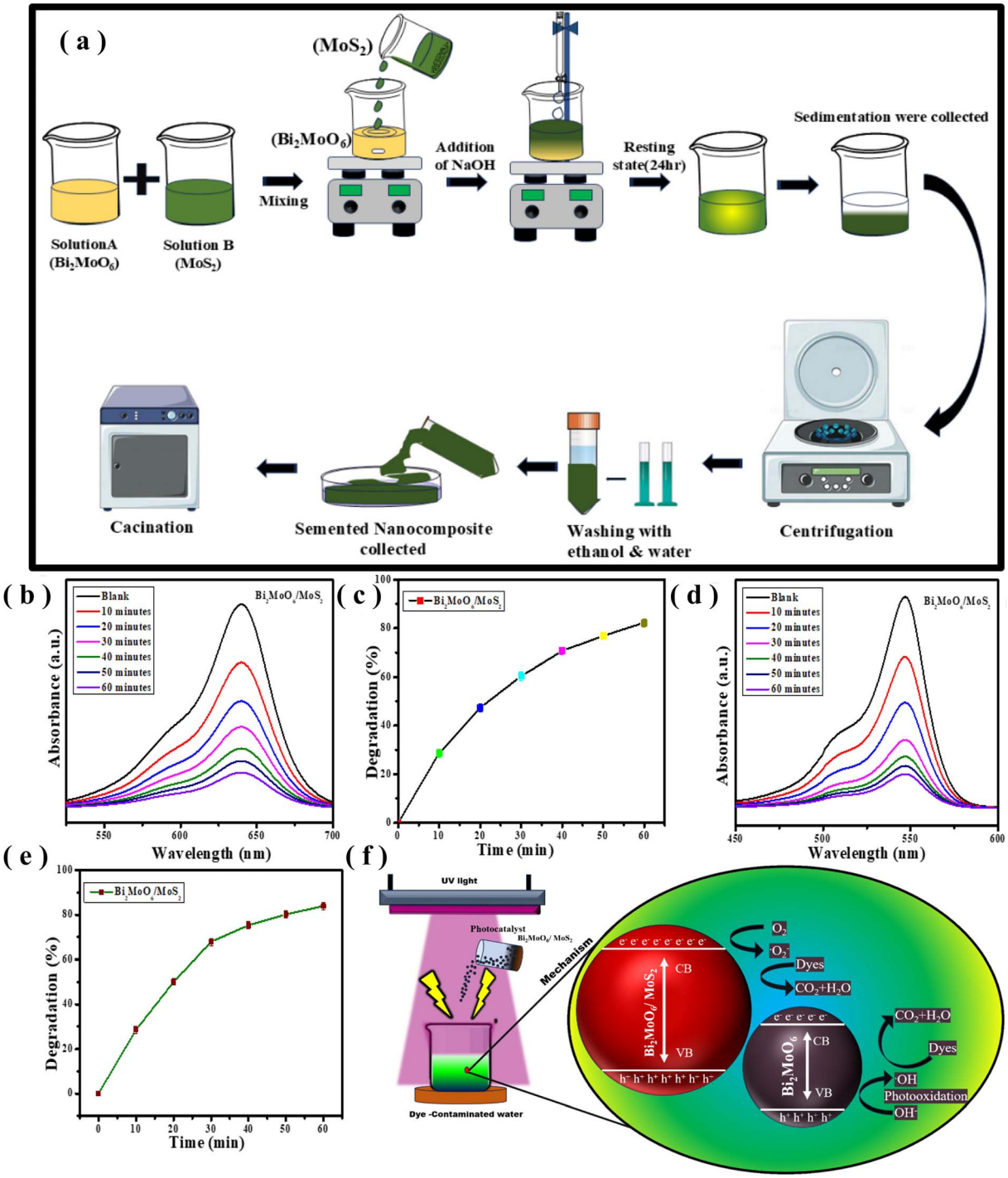

Fig. 4 (a) Synthesis method of Bi_2MoO_6/MoS_2 nanocomposite. (b) UV-Vis spectrum graphs showing the deterioration of dyes over various times. (c) Acid Blue dye's degradation percentage against time graphs demonstrate. (d) UV-Vis spectrum graphs showing the deterioration of dyes over various times. (e) Rose Bengal dye's degradation percentage against time graphs demonstrate. (f) Mechanism of photocatalytic activity of Bi_2MoO_6/MoS_2 nanocomposite. Reproduced from ref. 57 with permission from Elsevier. Copyright 2025.

the pH with NaOH, sedimentation, centrifugation, washing, and calcination. Fig. 4f illustrates the photodegradation mechanism of the Bi_2MoO_6/MoS_2 nanocomposite. The enhanced photocatalytic performance is attributed to the unique heterojunction structure, wide light absorption, and efficient charge separation; Bi_2MoO_6 generates electron–hole pairs, while MoS_2's layered structure facilitates charge transfer and inhibits recombination. Reactive oxygen species produced degrade dyes *via* oxidative cleavage of chromophoric groups, mineralizing them into non-toxic compounds.[57]

One of the primary advantages of the co-precipitation method is its cost-effectiveness and scalability, which make it attractive for large-scale synthesis. Moreover, the method enables uniform dispersion of multiple metal species at the molecular or atomic level, which is conducive to the formation of phase-pure or compositionally homogeneous products. When carefully optimized, the co-precipitation process can yield Bi_2MoO_6 materials with relatively small particle sizes, large surface areas, and good stoichiometric control—factors that are crucial for enhancing photocatalytic performance. Despite these merits, the co-precipitation method also presents several notable limitations. First, it is highly sensitive to process parameters, such as pH, stirring rate, temperature, and precursor concentration, which can lead to poor reproducibility and batch-to-batch variation. Second, agglomeration of particles during or after precipitation is a common issue, which may reduce the effective surface area and hinder photocatalytic activity. Third, the resulting materials often exhibit low crystallinity, requiring additional thermal treatment to improve crystal structure, which may in turn compromise surface area or induce particle growth.

2.5. Microwave-assisted synthesis technique

Microwave-assisted hydrothermal/solvothermal synthesis has emerged as a novel and efficient technique in the field of synthetic chemistry, offering significant advancements in the rapid preparation of nanomaterials. Unlike conventional hydrothermal or solvothermal methods that rely on conductive or convective heating, microwave heating employs alternating electromagnetic fields to induce molecular rotation and dipolar polarization, resulting in uniform and volumetric heating. This distinct heating mechanism accelerates both nucleation and crystal growth processes, enabling rapid synthesis of high-quality materials with improved crystallinity and reduced energy consumption.

Li *et al.* successfully prepared Bi/Bi_2MoO_6 hollow microsphere (BMO-HMS) composites *via* microwave-assisted synthesis followed by nitrogen annealing. The BMO-HMS composites exhibited enhanced photocatalytic degradation of RhB under visible light irradiation, achieving a maximum degradation efficiency of 91%, significantly outperforming pure Bi_2MoO_6. The incorporation of Bi improved light absorption, suppressed electron–hole recombination, and substantially enhanced the photocatalytic performance of the composite.[58] The $Ag/Bi_2MoO_6/ZnO$ ternary heterojunction photocatalyst was synthesized *via* a two-step microwave-assisted hydrothermal method (Fig. 5a), showing superior degradation of LFX with an 86.4% removal rate, surpassing pure Bi_2MoO_6 and ZnO by 3 and 7 times, respectively. As shown in Fig. 5b and c, PL and transient photocurrent response curves demonstrated enhanced charge separation and reduced electron–hole recombination in the composite, aided by Ag nanoparticles acting as electron pumps. EIS confirmed lower charge transfer resistance in $Ag/Bi_2MoO_6/ZnO$ (Fig. 5d). Under light irradiation, electrons transfer from Bi_2MoO_6 to ZnO, while holes migrate oppositely; Ag nanoparticles facilitate this charge flow. Reactive oxygen species, especially $^1O_2$, $^{\bullet}OH$, and $^{\bullet}O_2^-$, play key roles in LFX degradation, producing harmless end products (Fig. 5e).[59]

The advantages of microwave-assisted synthesis are multifold: it not only shortens reaction times significantly but also enhances product yield and selectivity while minimizing by-product formation. Such characteristics make it especially beneficial for materials that are highly sensitive to reaction parameters, allowing precise control over morphology and phase purity. However, this method also has inherent limitations. The efficiency of microwave heating depends heavily on the presence of polar molecules such as water or ethanol in the reaction medium, as nonpolar solvents are less responsive to microwave irradiation and may adversely affect the uniformity of heating, consequently impacting product size and shape. Additionally, factors such as solvent volume and the dielectric properties of the reaction vessel can influence the distribution of the electromagnetic field, necessitating careful optimization of reaction conditions.

2.6. Sol–gel method

The sol–gel method stands as a versatile and widely adopted chemical synthesis technique, renowned for its exceptional capability in producing high-purity and homogeneous materials at relatively low temperatures. In contrast to many top-down approaches that break down bulk materials, the sol–gel process is a bottom-up method, building materials from molecular precursors. It typically involves the transition of a system from a liquid "sol" (a colloidal suspension of solid particles) into a solid "gel" network.[60] This distinctive mechanism allows for precise control over the chemical composition, microstructure, and porosity of the final product. Consequently, the sol–gel technique enables the fabrication of a wide range of advanced materials, including uniform nanoparticles, thin films, and monolithic aerogels, with tailored properties for specific applications.[61]

Sun *et al.* optimized the photocatalytic performance of Bi_2MoO_6-based catalysts by systematically varying the calcination temperature during sol–gel synthesis. Calcination temperature was identified as a key parameter affecting the crystallinity and bandgap of Bi_2MoO_6. Notably, spherical Bi_2MoO_6 synthesized at 450 °C exhibited the highest photocatalytic efficiency for phenol degradation. Under visible light irradiation for 5 hours, the photocatalyst achieved approximately 99.3% degradation of phenol, demonstrating excellent activity.[62] Zhu *et al.* successfully synthesized an $AgI–Bi_2MoO_6/$vermiculite composite photocatalyst *via* a combined sol–gel and

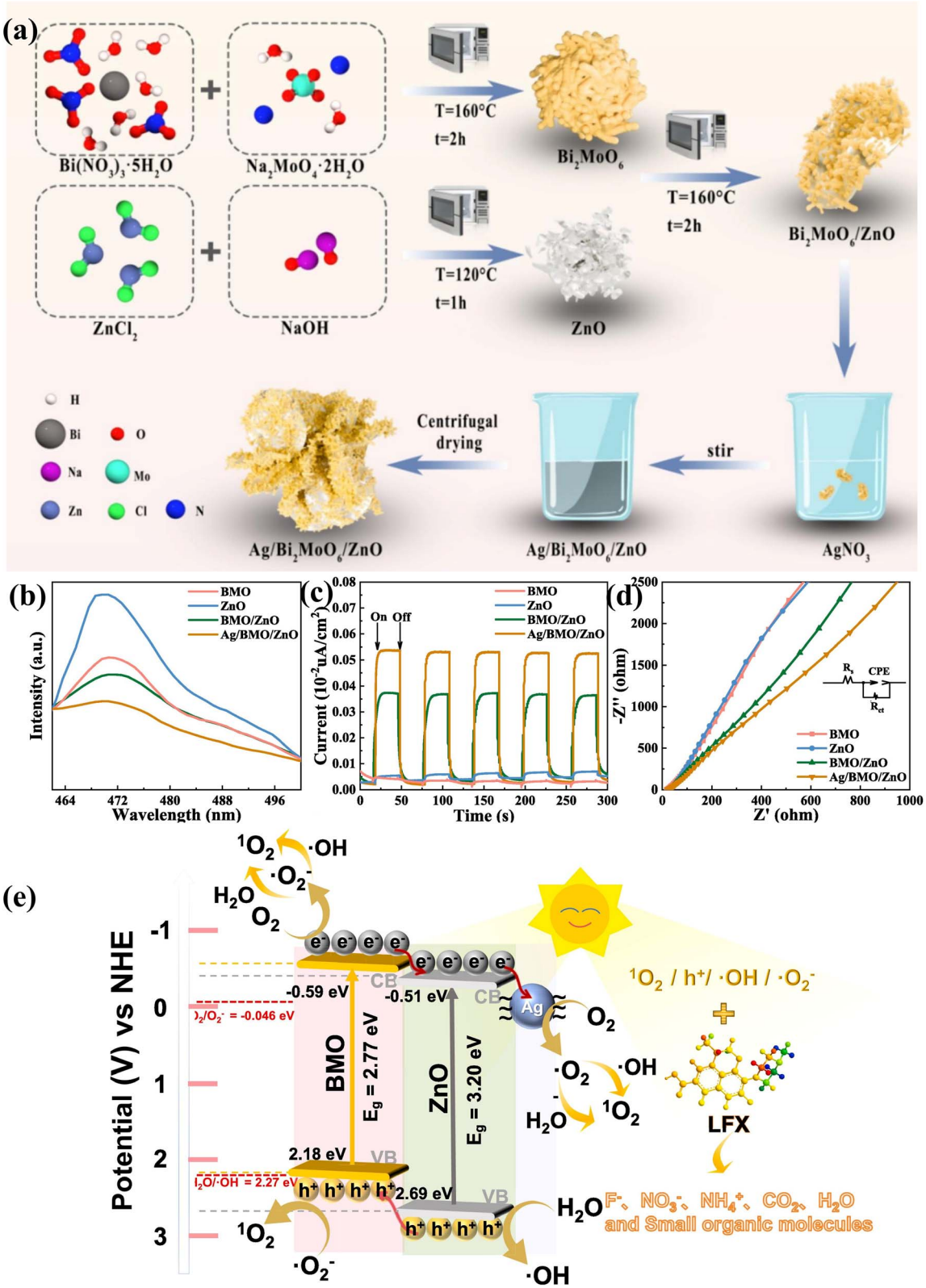

Fig. 5 (a) The schematic illustration of the synthesis process of the ternary Ag/Bi_2MoO_6/ZnO. (b) PL spectra, (c) transient photocurrent response curves, (d) EIS spectra. (e) The schematic photocatalytic mechanism of LFX degradation by Ag/Bi_2MoO_6/ZnO heterojunction. Reproduced from ref. 59 with permission from Elsevier. Copyright 2024. Note: "BMO" in this figure denotes Bi_2MoO_6.

precipitation method. Compared to pure Bi_2MoO_6 and Bi_2MoO_6/vermiculite composites, the AgI–Bi_2MoO_6/vermiculite exhibited significantly enhanced photocatalytic degradation efficiency toward malachite green (MG) dye. Both Bi_2MoO_6 and AgI were uniformly dispersed on the vermiculite surface, resulting in a stable structure with improved adsorption capacity. Furthermore, the composite demonstrated an extended visible-light absorption range and accelerated electron–hole separation, contributing to its superior photocatalytic performance.[63] Nguyen Trung *et al.* synthesized Bi Z-type heterojunctions *via* a combination of solvothermal and sol–gel methods. The resulting heterojunctions exhibited enhanced photocatalytic activity, which was attributed to the efficient separation of photogenerated charge carriers within the heterojunction structure.[64] In another study, a 3D $SrTiO_3$/Bi_2MoO_6 heterojunction photocatalyst was fabricated *via* sol–gel and impregnation methods to enhance visible-light-driven overall water splitting (Fig. 6a). Among various compositions, 50% ST/BM exhibited the highest hydrogen (3350 μmol) and oxygen (1875 μmol) evolution, with excellent stability over five cycles. As shown in Fig. 6c–e, characterizations (PL, EIS, Mott–Schottky) confirmed strong interfacial contact, efficient charge transfer, and reduced electron–hole recombination. The heterojunction promoted band alignment: holes transferred from $SrTiO_3$ to Bi_2MoO_6, while electrons moved oppositely, enhancing charge separation (Fig. 6b).[65]

Jia *et al.* successfully synthesized $CuFeO_4$/Bi_2MoO_6 composite materials by loading $CuFeO_4$ nanoparticles onto the surface of Bi_2MoO_6 microflowers *via* a facile sol–gel combined with hydrothermal method. The strong interfacial interaction between $CuFeO_4$ and Bi_2MoO_6 resulted in an increased specific surface area and enhanced porosity, providing abundant active sites for metal ion reactions and facilitating charge transfer. Furthermore, the intimate contact between the two components promoted efficient charge carrier separation and suppressed electron–hole recombination. Consequently, the optimized CBM-10 catalyst achieved a remarkable LFX degradation efficiency of 95.1% within 60 minutes under photocatalytic conditions.[66]

The sol–gel method presents a highly advantageous and versatile route for the synthesis of Bi_2MoO_6-based photocatalytic materials, primarily due to its exceptional capability for precise compositional and structural control. The foremost merits of this technique include: (1) Precise stoichiometric control through molecular-level mixing of precursors, which ensures a uniform elemental distribution and is crucial for obtaining phase-pure Bi_2MoO_6; (2) facile compositional engineering, as the liquid-phase process allows for the effortless incorporation of dopants (*e.g.*, rare earth metals) or the formation of intimate heterojunctions with other semiconductors, enabling tailored optoelectronic properties; and (3) versatile material architecture, permitting the synthesis of diverse morphologies such as porous xerogels and aerogels that offer

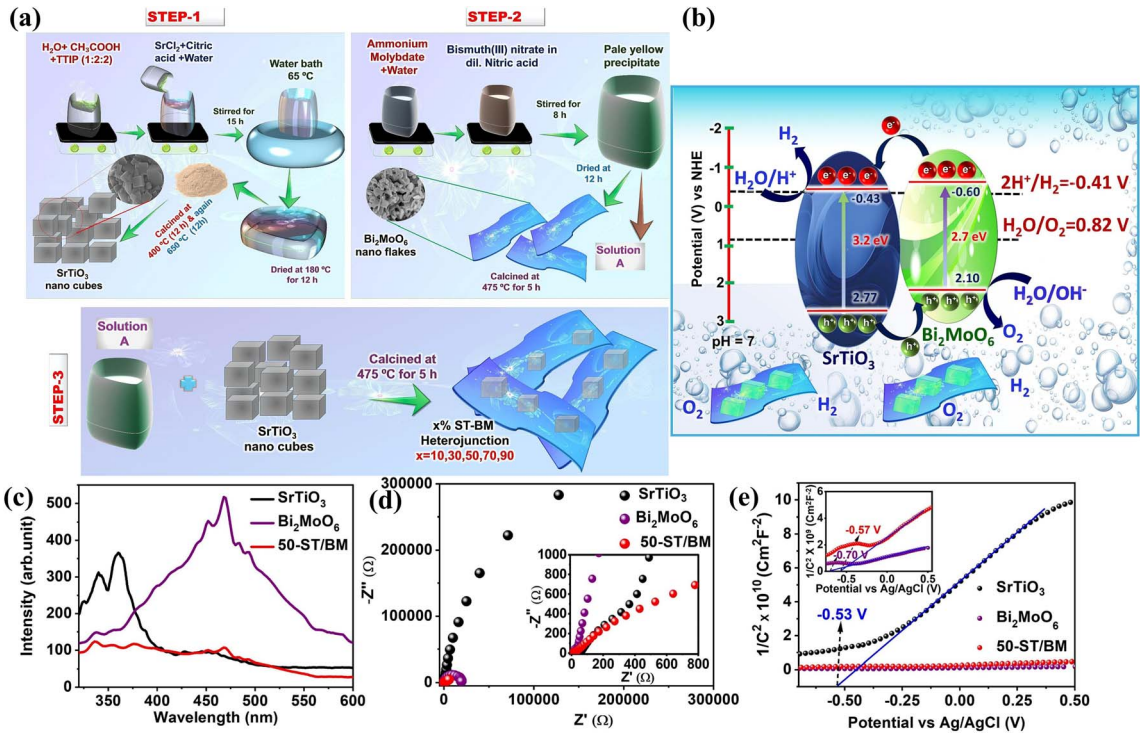

Fig. 6 (a) Overall synthesis procedure for 3D $SrTiO_3$ nanocubes (step 1), 2D Bi_2MoO_6 nanoflakes (step 2), and x% $SrTiO_3$/Bi_2MoO_6 heterojunction nanocomposite (step 3). (b) The photocatalytic overall water splitting mechanism of 50-$SrTiO_3$/Bi_2MoO_6 nanocomposite. (c) PL spectra (d) EIS Nyquist plots and (e) the Mott–Schottky plots of $SrTiO_3$, Bi_2MoO_6, and 50-$SrTiO_3$/Bi_2MoO_6 nanocomposite. Reproduced from ref. 65 with permission from Elsevier. Copyright 2025. Note: "ST/BM" in this figure denotes $SrTiO_3$/Bi_2MoO_6.

high specific surface areas, thereby providing abundant active sites for photocatalytic reactions. However, the application of the sol–gel method is accompanied by several inherent challenges: the process often involves a lengthy synthesis cycle with aging and drying steps; the reliance on metal–organic precursors can lead to high costs and environmental concerns; and the requisite calcination step must be meticulously controlled to prevent particle agglomeration and the consequent loss of surface area. Despite these limitations, the unparalleled control over material chemistry and microstructure makes sol–gel synthesis a powerful and widely adopted strategy for the fundamental research and development of high-performance Bi_2MoO_6-based photocatalysts.

3. Construction of Bi_2MoO_6 matrix composites

Although Bi_2MoO_6 is a promising photocatalyst due to its unique layered structure, the single-component material suffers from several limitations, including low quantum yield, rapid recombination of photogenerated electron–hole pairs, and poor charge transport efficiency.[67] To overcome these bottlenecks, researchers have focused on optimizing their photocatalytic performance through a variety of strategies in recent years.

3.1. Heterojunction construction

An ideal semiconductor photocatalyst should possess a broad visible-light absorption range, efficient charge separation and transport, as well as strong redox capabilities. While narrow-bandgap materials exhibit excellent light absorption, their limited redox potentials motivate the search for wide-bandgap semiconductors with suitably positioned CB and valence bands (VB). However, a single semiconductor often fails to meet the complex demands of photocatalytic reactions, leading to the development of semiconductor heterojunction composites. Constructing such heterojunctions effectively suppresses the rapid recombination of photogenerated charge carriers, thereby enhancing photocatalytic efficiency through band structure optimization and extended photoresponse.[68] Therefore, constructing heterojunctions is an effective strategy to expand the applicability of photocatalysts. By forming heterojunctions with other semiconductor materials, Bi_2MoO_6 can modulate interfacial electron transfer, thereby promoting the separation and migration of photogenerated charge carriers.[69] Bi_2MoO_6-based heterojunctions can be classified into four configurations: type I heterojunction (Fig. 7a), type II heterojunction (Fig. 7b), Z-scheme heterojunctions (Fig. 7c and d), and S-scheme heterojunctions. Among these, S-scheme and Z-scheme heterojunctions have garnered significant attention in recent research owing to their enhanced redox capabilities.

The Z-scheme heterojunction exhibits a unique charge transfer mechanism that offers significant advantages over conventional Type I and II heterostructures. In this system, photogenerated electrons in the lower CB of one semiconductor recombine with holes in the higher VB of an adjacent semiconductor, thereby preserving holes with stronger oxidation potential in the lower VB and electrons with higher reduction potential in the higher CB. This selective interfacial charge recombination pathway combines efficient carrier separation with superior redox potentials compared to Type I/II heterojunctions, addressing a key limitation of traditional heterostructure designs.

3.1.1 All-solid-state Z-scheme heterojunctions. The all-solid-state Z-scheme configuration employs solid electron mediators (*e.g.*, Au, Ag, Pt, or graphene-based materials) as electron bridges to enable Z-scheme transfer while suppressing backward recombination. However, this approach faces

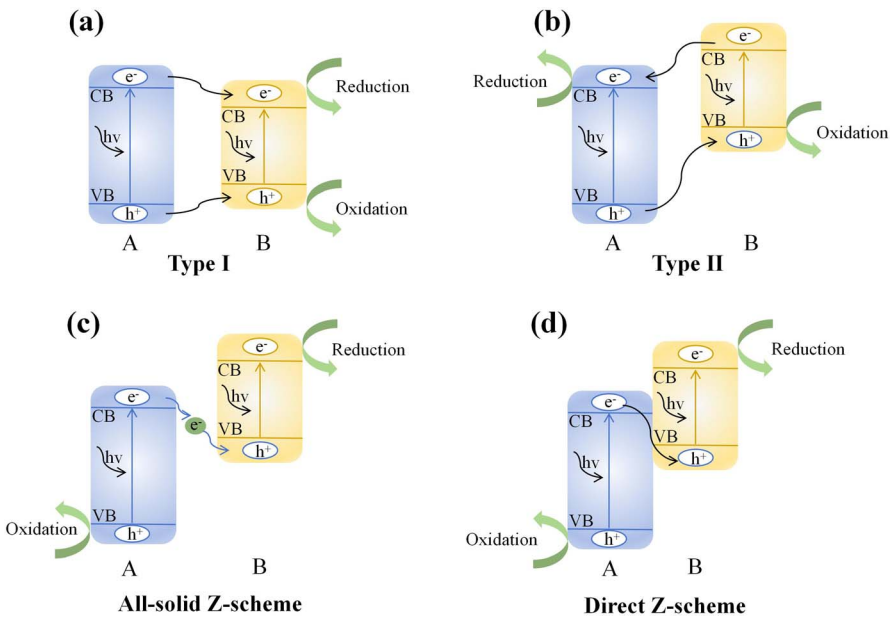

Fig. 7 Diagram of heterojunction structure.

challenges, including the difficulty of precisely controlling mediator distribution at the interface, high material costs, and partial blockage of incident light by opaque mediators.

Ma *et al.* synthesized an all-solid Z-type Bi_2MoO_6/CNTs/g-C_3N_4 composite and systematically investigated the effect of g-C_3N_4 content by preparing composites with varying molar ratios of g-C_3N_4 to Bi_2MoO_6 (25%, 50%, 75%, and 100%). These ternary composites were designated as MTN25, MTN50, MTN75, and MTN100, respectively. To elucidate the structural and compositional features, the morphology and elemental distribution of pristine Bi_2MoO_6 and the MTN75 composite were characterized by SEM, EDX, and HR-TEM (Fig. 8a–f). The photocatalytic degradation and debromination of 2,4-dibromophenol followed a Z-scheme mechanism (Fig. 8g). Under visible light irradiation, photoexcited electrons and holes are generated in both g-C_3N_4 and Bi_2MoO_6. The presence of CNTs as an electron mediator facilitates rapid electron transfer from the CB of Bi_2MoO_6 (PS II) to the VB of g-C_3N_4 (PS I). This carrier migration results in electron accumulation in the CB of g-C_3N_4 and hole accumulation in the VB of Bi_2MoO_6. The CB potential of g-C_3N_4 is located at −1.33 V, while the VB of Bi_2MoO_6 is at +3.21 V *versus* the normal hydrogen electrode (NHE). Electrons accumulated in the CB of g-C_3N_4 drive the reduction of Bi_2 to Br^-, promoting the conversion of bromine into bromide ions and producing monobrominated and debrominated intermediates during the initial photocatalytic stage. Concurrently, holes concentrated in the VB of Bi_2MoO_6 oxidize these intermediates *via* radical pathways. Given the matched Fermi levels of g-C_3N_4 and Bi_2MoO_6, CNTs serve as efficient charge-transfer channels. Consequently, the optimized Bi_2MoO_6/CNTs/g-C_3N_4 composite exhibits significantly enhanced photocatalytic degradation efficiency compared to pristine Bi_2MoO_6 and g-C_3N_4.[70]

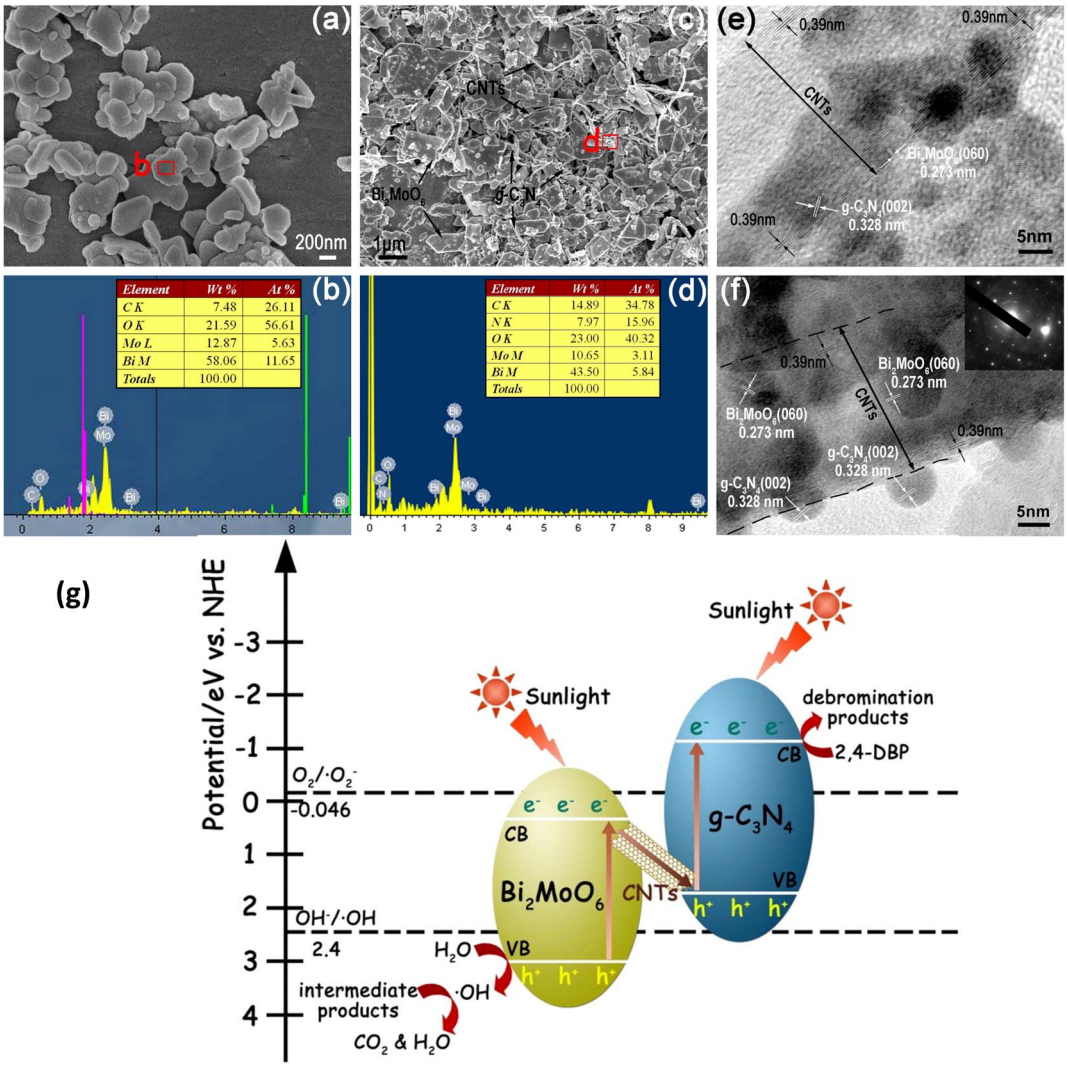

Fig. 8 SEM images of (a) Bi_2MoO_6 and (c) MTN75 composite, and the accompanying EDX spectra (the marked area b and d) of (b) Bi_2MoO_6 and (d) MTN75 composite. HRTEM images of MTN75 composite (e) and (f), and the inset of (f) is the SAED pattern of the MTN75 composite; (g) photocatalytic mechanism scheme of all-solid-state Z-scheme MTN75 composite. Reproduced from ref. 70 with permission from Elsevier. Copyright 2017.

3.1.2 Direct Z-scheme heterojunctions. Direct Z-scheme heterojunctions eliminate the need for intermediate electron mediators by establishing intimate contact between semiconductors with properly aligned band structures and Fermi levels. This direct coupling configuration offers multiple advantages: shortened charge transfer distances, formation of built-in electric fields to accelerate carrier separation, and full retention of the constituent materials' redox potentials. The absence of additional mediator materials not only simplifies the fabrication process but also enhances light utilization efficiency. The simplified fabrication and improved light absorption make direct Z-scheme systems a research priority, though their formation requires precise control of interfacial atomic and electronic structures.

A direct Z-scheme heterojunction photocatalyst was successfully constructed by integrating Bi_2MoO_6 nanoparticles with NiFe-layered double hydroxide (NiFe-LDH) nanoflowers. The optimized BMO/NiFe15 composite demonstrated exceptional photocatalytic activity, achieving 95% degradation of tetracycline (TC) within 120 minutes under visible light, with a reaction rate constant ($0.0219\ min^{-1}$) 4.2 and 8.4 times higher than that of pure BMO and NiFe, respectively. The outstanding performance is attributed not only to the enhanced visible light absorption and the larger specific surface area but also to the ingeniously designed Z-scheme charge transfer mechanism at the heterojunction interface. This unique pathway efficiently directs the recombination of useless electrons in the conduction band (CB) of NiFe with holes in the valence band (VB) of BMO at the interface, thereby preserving the most powerful photoinduced electrons in the CB of BMO and holes in the VB of NiFe. Consequently, the composite retains strong redox capabilities: the electrons in BMO's CB (−0.34 eV *vs.* NHE) can reduce O_2 to generate superoxide ($^{\bullet}O_2^-$), while the holes in NiFe's VB (3.16 eV *vs.* NHE) possess sufficient potential to oxidize H_2O/OH^- to form hydroxyl ($^{\bullet}OH$). This spatially directed separation of charge carriers drastically suppresses the recombination of electron–hole pairs, as confirmed by significantly quenched PL intensity and improved photocurrent response.[71]

Fu *et al.* engineered a direct Z-scheme heterojunction composed of 2D Bi_2O_3 nanosheets and 3D Bi_2MoO_6 microspheres, which exhibited outstanding visible-light photocatalytic performance, achieving 96.4% phenol degradation and a hydrogen evolution rate of 52 μmol g^{-1}. This enhancement is attributed to spatially separated redox sites, improved light absorption, and efficient charge transport.[72] Direct Z-type $Bi_2MoO_6/CoWO_4$ (BMC-*x*) heterostructures, characterized by high redox potential, have been employed for the photodegradation of norfloxacin (NOR). Pure Bi_2MoO_6 consists of interlaced spheres assembled from nanosheets approximately 2 μm in diameter (Fig. 9a and f), while pure $CoWO_4$ is composed

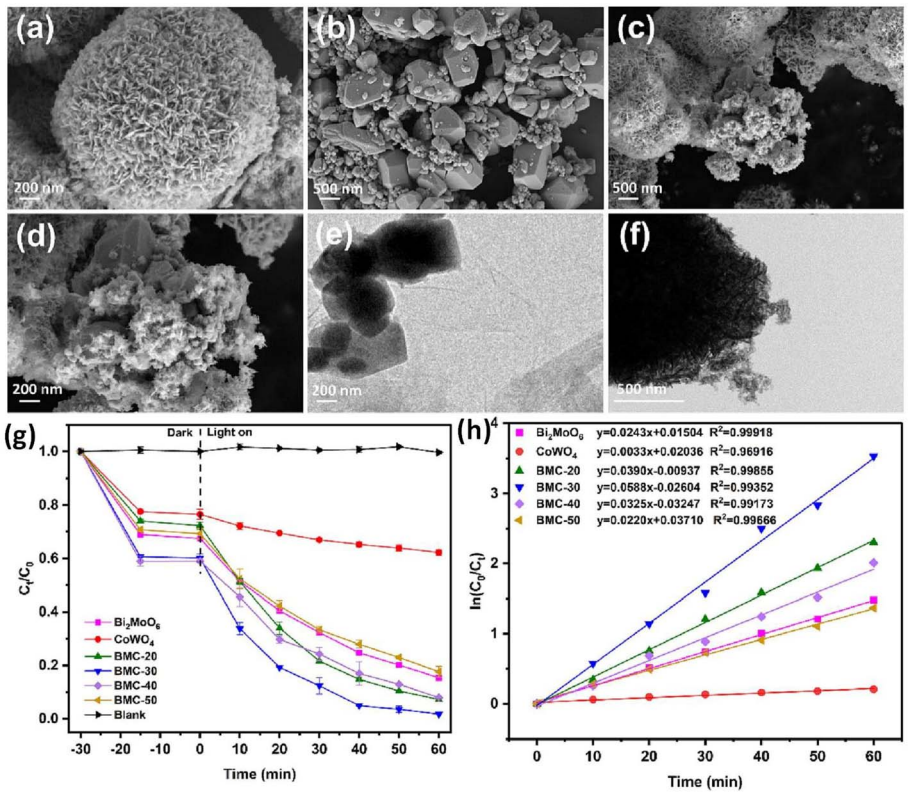

Fig. 9 (a) SEM images of Bi_2MoO_6, (b) $CoWO_4$, (c and d) BMC-30 composites, (e) TEM images of $CoWO_4$, (f) Bi_2MoO_6. Reproduced with permission. (g) Photocatalytic degradation, (h) and the corresponding *k* values of NOR by various samples under visible light. (Conditions: photocatalyst = 400 mg L^{-1}, $[NOR]_0$ = 10 mg L^{-1}, temperature = 25 ± 0.5 °C). Reproduced from ref. 73 with permission from Elsevier. Copyright 2023.

of irregular nanoparticles exhibiting good crystallinity (Fig. 9b and e). In the BMC-$_{30}$ nanocomposite (Fig. 9c and d), Bi_2MoO_6 nanosheets primarily cover $CoWO_4$ particles, attributable to the *in situ* growth process. Elemental mapping confirms the uniform distribution of W, Mo, Co, O, Bi, and C across the BMC-30 surface. Under visible light irradiation, BMC-*x* composites demonstrate excellent photodegradation performance toward NOR. As shown in Fig. 9g and h, after 60 minutes of illumination, the NOR degradation efficiency of BMC-30 reached 97.1%, with an apparent rate constant of 0.0588 min^{-1}.[73]

Liu *et al.* constructed an efficient Bi-based Z-type Bi_3O_4Cl/Bi_2MoO_6 photocatalytic system by employing a coordinated *in situ* growth method, where Bi_2MoO_6 was directly synthesized on Bi_3O_4Cl. This *in situ* growth formed a porous and intimate interface between Bi_2MoO_6 and Bi_3O_4Cl nanoparticles, facilitating effective photogenerated electron transfer channels and establishing the Z-type heterojunction framework. During photocatalytic degradation, photogenerated holes were identified as the primary reactive species, while $^{\bullet}O_2^-$ and $^{\bullet}OH$ radicals contributed comparably to the degradation process.[74]

3.1.3 S-scheme heterojunctions. S-scheme heterojunctions consist of two semiconductors with distinct band structures that form atomic–scale interfaces. This configuration generally combines a reductive photocatalyst (with a small work function and high Fermi level) and an oxidative photocatalyst (with a large work function and low Fermi level), facilitating directional charge transfer to enhance redox capabilities. The formation of an internal electric field drives photogenerated electrons from the oxidative photocatalyst (OP) to the reductive photocatalyst (RP). The contact between the two semiconductor interfaces causes band bending and under the action of the coulomb force of the electron holes, the photogenerated electrons of the OP and the holes of the RP are recombined at the interface position, thus achieving strong redox ability and effective separation of the electron hole pairs (Fig. 10). Owing to the distinctive electron migration pathway of the S-type heterojunction, photogenerated carriers can be effectively separated and utilized while preserving the material's optimal redox capability.[75]

As an advanced alternative to the all-solid-state Z-scheme, the S-scheme (Step-scheme) heterojunction design offers significant performance and practicality advantages for enhancing Bi_2MoO_6-based photocatalysts, while retaining the core benefit of strong redox power preservation. The key distinctions lie in three primary aspects. First, the all-solid-state Z-scheme relies heavily on an external electron mediator (*e.g.*, Au, graphene) to facilitate charge transfer. Conversely, the S-scheme achieves directional charge flow through internally driven forces, primarily the built-in electric field (IEF), band bending, and coulombic attraction. This mediator-free mechanism inherently circumvents associated performance losses, including light absorption competition and inefficient interfacial charge hopping. Second, while both strategies preserve potent charge carriers, the S-scheme provides a more direct and rational charge transfer pathway from the perspectives of energy band theory and interface electrostatics. Finally, in terms of practicality and design, the S-scheme configuration is generally simpler and more cost-effective to fabricate, as it avoids the complex process of embedding noble metal mediators.[76] This mediator-free approach results in superior light utilization, more efficient charge dynamics, and ultimately, a more robust and high-performing photocatalyst for environmental remediation applications.

Yao *et al.* successfully constructed an S-scheme $CdIn_2S_4$/Bi_2MoO_6 heterojunction photocatalyst driven by a built-in electric field (IEF). Under simulated sunlight, the 25%-$CdIn_2S_4$/Bi_2MoO_6 composite achieved an impressive degradation efficiency of 93.7% for levofloxacin (LFX) within 90 minutes. Free radical trapping and electron spin resonance (ESR) tests confirmed that $^{\bullet}OH$ and $^{\bullet}O_2^-$ are the primary active species responsible for the degradation. In-depth analysis suggests that the oxygen vacancy defects likely present on the Bi_2MoO_6 surface play a crucial role: they act as electron capture centers, effectively suppressing the recombination of photogenerated electron–hole pairs and providing more sites for

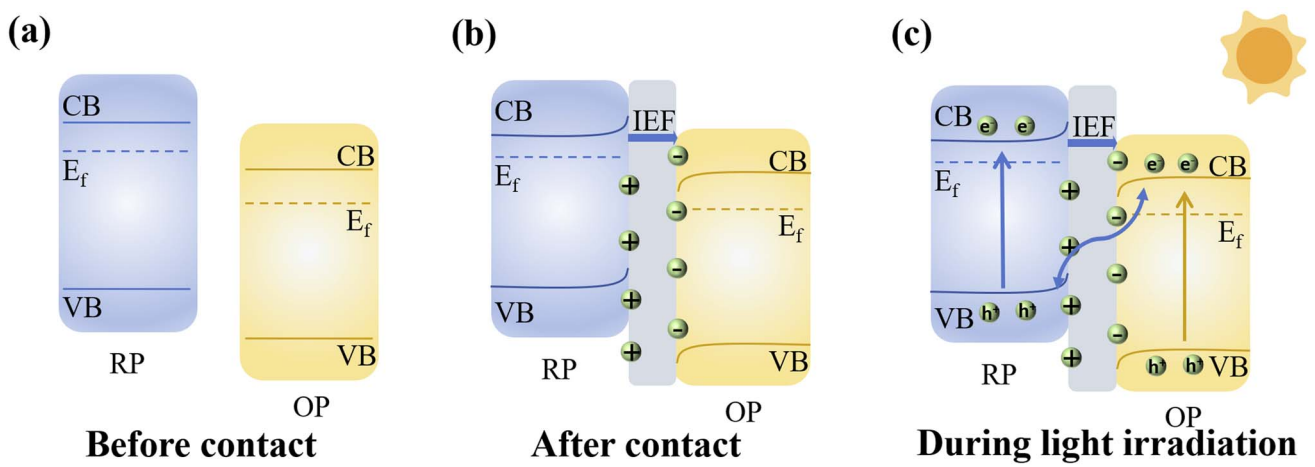

Fig. 10 Schematic of charge transfer of S-scheme heterojunction.

molecular oxygen activation. Building upon this, the S-scheme heterostructure establishes efficient spatial separation channels for charge carriers. Driven by the IEF, electrons in the CB of Bi_2MoO_6 recombine with holes in the VB of $CdIn_2S_4$ at the interface. This process selectively enriches highly reductive electrons in the CB of $CdIn_2S_4$ and retains highly oxidative holes in the VB of Bi_2MoO_6. The synergistic effect between these oxygen vacancy defects and the S-scheme heterojunction collectively enables the highly efficient separation and migration of photogenerated carriers while maximizing the redox potential of the system, thereby significantly enhancing the photocatalytic degradation efficiency of LFX.[77] Chen *et al.* assembled Bi_2WO_6 nanoplates and Bi_2MoO_6 nanoparticles into hollow microspheres with a unique fractal structure, which were then anchored onto reduced graphene oxide (RGO) to form a ternary S-type RGO-Bi_2MoO_6/Bi_2WO_6 heterojunction. This composite exhibited significantly enhanced RhB degradation efficiency under visible light irradiation, along with improved photo-corrosion stability.[78] Zhen *et al.* synthesized a g-C_3N_4/Bi_2MoO_6 S-scheme heterojunction that demonstrated enhanced photocatalytic degradation of phenol and hydrogen evolution under visible light irradiation. In this S-scheme composite, the internal electric field, band bending, and interfacial charge attraction between g-C_3N_4 and Bi_2MoO_6 synergistically promote efficient separation of photogenerated electrons and holes. This effective charge separation preserves the strong redox capabilities of both components, contributing to the improved photocatalytic performance.[79]

Wang *et al.* employed a facile hydrothermal method to construct 2D/2D S-scheme Fe_2O_3/Bi_2MoO_6 heterojunctions. Under low-concentration H_2O_2, the composite with 0.5 wt% Fe_2O_3 achieved TC degradation rates 3.2 times higher than pure Fe_2O_3 and 2.0 times higher than pure Bi_2MoO_6. The photocatalytic activity of Fe_2O_3/Bi_2MoO_6 was significantly enhanced due to improved charge carrier separation, as evidenced by PL spectra, photocurrent response, and EIS analysis (Fig. 11a–c). Fig. 11d–f shows the possible S-scheme charge transfer mechanism between Fe_2O_3 and Bi_2MoO_6 under light irradiation. The 2D/2D S-scheme heterojunction between Fe_2O_3 and Bi_2MoO_6 facilitated efficient electron–hole separation, with electrons transferring from Bi_2MoO_6's CB to Fe_2O_3's VB under an internal electric field, preserving highly reactive carriers (CB electrons of Fe_2O_3 and VB holes of Bi_2MoO_6). Additionally, the photo-Fenton reaction further boosted TC degradation by generating $^{\bullet}OH$ *via* Fe^{3+}/Fe^{2+} cycling, while the 2D/2D structure shortened charge transfer distances and provided abundant active sites. The system achieved high efficiency with minimal H_2O_2 (30 μL), demonstrating superior catalytic performance compared to pure photocatalysis(Fig. 11g).[80]

3.2. Ion doping

Doping strategies are typically categorized into non-metal doping and metal doping. Non-metal doping involves elements such as carbon (C), nitrogen (N), phosphorus (P), sulfur (S), halogens, and other non-metallic atomic groups. These dopants can modify the electronic structure and enhance light absorption. Metal doping, on the other hand, focuses on transition metal ions, which possess distinctive electron configurations. When doped into Bi-based materials, these metal ions can interact with the 6p orbitals of Bi, facilitating the formation of crossover energy levels. This interaction significantly promotes the separation and migration of photogenerated charge carriers, thereby improving photocatalytic performance.

In addition to single-element doping, co-doping strategies—where two or more different types of ions are simultaneously introduced into a material—have garnered significant attention for enhancing photocatalytic performance. Co-doping enables the synergistic integration of distinct ionic characteristics. For example, doping ions with varying valence states can substitute lattice ions to enhance electrical conductivity, while differences in ionic radii can create migration barriers that suppress interstitial defects or ion interdiffusion within the structure. Multi-ion co-doping is particularly effective in extending visible light absorption and boosting the capacity of photocatalysts to store and transfer photogenerated electrons or protons. This enhances charge carrier separation and reduces recombination losses, leading to improved photocatalytic efficiency. However, the introduction of multiple dopants also increases the complexity of the synthesis process. Precise control over the chemical compatibility, concentration, and spatial distribution of each dopant is essential to avoid undesirable phase separation or performance degradation, making the fabrication process more challenging.

3.2.1 Metal ion doping strategy. Wang *et al.* synthesized a series of Sm-doped Bi_2MoO_6 photocatalysts with varying Sm contents using a simple aqueous method. They observed that increasing the Sm doping concentration resulted in a gradual narrowing of the band gap energy, thereby enhancing the catalyst's ability to absorb visible light. The photocatalytic performance was found to be highly dependent on the Sm concentration, with 0.8 at% Sm-doped Bi_2MoO_6 showing the most efficient activity—achieving 89% degradation of RhB within 50 minutes under visible-light irradiation. The enhanced activity was attributed to Sm ions functioning as effective electron traps, which suppressed electron–hole recombination and promoted visible-light-driven photocatalytic reactions.[81] Guo *et al.* incorporated Fe^{3+} ions into the crystal lattice of Bi_2MoO_6 to synthesize *x*Fe-Bi_2MoO_6 photocatalysts and systematically investigated the influence of Fe^{3+} doping concentration on photocatalytic performance. They discovered a strong correlation between the Fe^{3+} content and the material's photocatalytic activity: as the doping concentration increased, the VB edge shifted downward, effectively narrowing the band gap (Fig. 12a and b). This modification enhanced visible-light absorption. Furthermore, the synergistic effect between Fe^{3+} ions and the intrinsic multilayered structure of Bi_2MoO_6 facilitated faster charge separation and improved surface reaction efficiency. As a result, the doped photocatalysts exhibited superior light-harvesting capabilities and enhanced photocatalytic performance compared to undoped Bi_2MoO_6 (Fig. 12c).[82] Xu *et al.* developed a Cd-doped Bi_2MoO_6 photocatalyst and evaluated its efficiency for the degradation ofloxacin under visible light. As

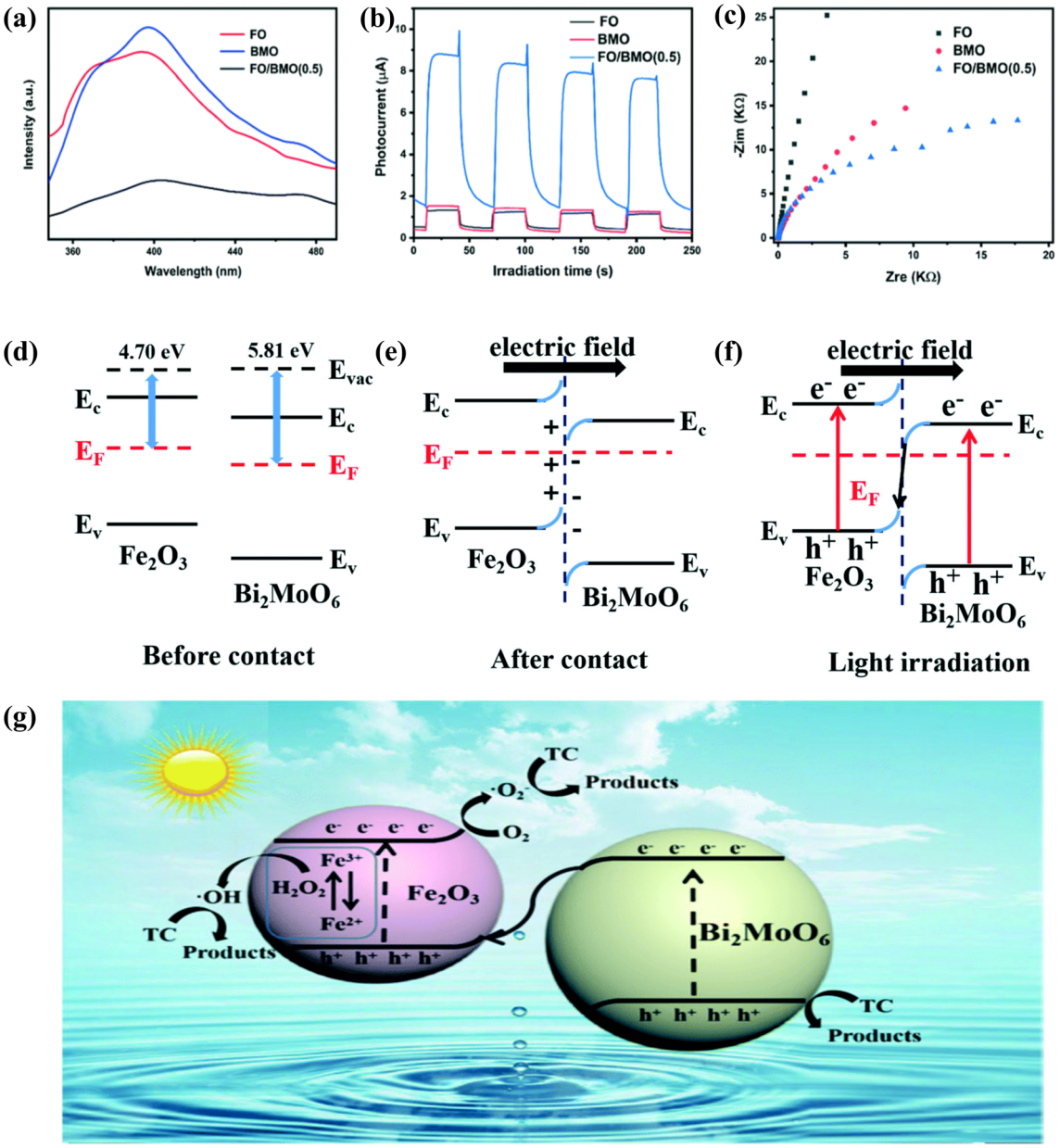

Fig. 11 (a) PL emission spectra for Fe_2O_3, Bi_2MoO_6, and Fe_2O_3/Bi_2MoO_6 (0.5) photocatalysts. The wavelength of excitation light for fluorescence emission spectra was 327 nm. (b) Transient photocurrent responses for the Fe_2O_3, Bi_2MoO_6 and Fe_2O_3/Bi_2MoO_6 (0.5) composite. (c) EIS Nyquist plots of Fe_2O_3, Bi_2MoO_6 and the Fe_2O_3/Bi_2MoO_6 (0.5) composite. (d) The work functions of Fe_2O_3 and Bi_2MoO_6 before contact. (e) The internal electric field and band edge bending at the interface of Fe_2O_3/Bi_2MoO_6 after contact. (f) The S-scheme charge transfer mechanism between Fe_2O_3 and Bi_2MoO_6 under light irradiation. (g) Schematic diagram of the photo-Fenton catalytic oxidation of TC over Fe_2O_3/Bi_2MoO_6 (0.5) under visible-light irradiation ($\lambda \geq 420$ nm). Reproduced from ref. 80 with permission from Royal Society of Chemistry. Copyright 2021. Note: "BMO" in this figure denotes Bi_2MoO_6. "FO" in this figure denotes Fe_2O_3.

shown in Fig. 12d–i, the 1% Cd-doped Bi_2MoO_6 photocatalyst demonstrated significantly enhanced charge separation efficiency, as evidenced by its photocurrent density (0.48 μA cm^{-2}) being twice that of pure Bi_2MoO_6 and five times higher than $CdMoO_4$, along with reduced fluorescence intensity indicating suppressed charge recombination. While maintaining similar light absorption characteristics with an edge at 506 nm, the doped material exhibited a slightly widened bandgap and more positive CB position, which collectively improved charge separation despite a marginal decrease in $^{\bullet}O_2^-$ generation capacity. These modified electronic properties, confirmed through Mott–Schottky and DRS analyses, contributed to the enhanced photocatalytic degradation efficiency of ofloxacin by effectively suppressing charge recombination while preserving sufficient light absorption capability.[83]

Alemi *et al.* synthesized a series of Bi_2MoO_6 photocatalysts doped with rare earth ions (Gd^{3+}, Ho^{3+}, Yb^{3+}) and investigated their structural and photocatalytic properties. The results

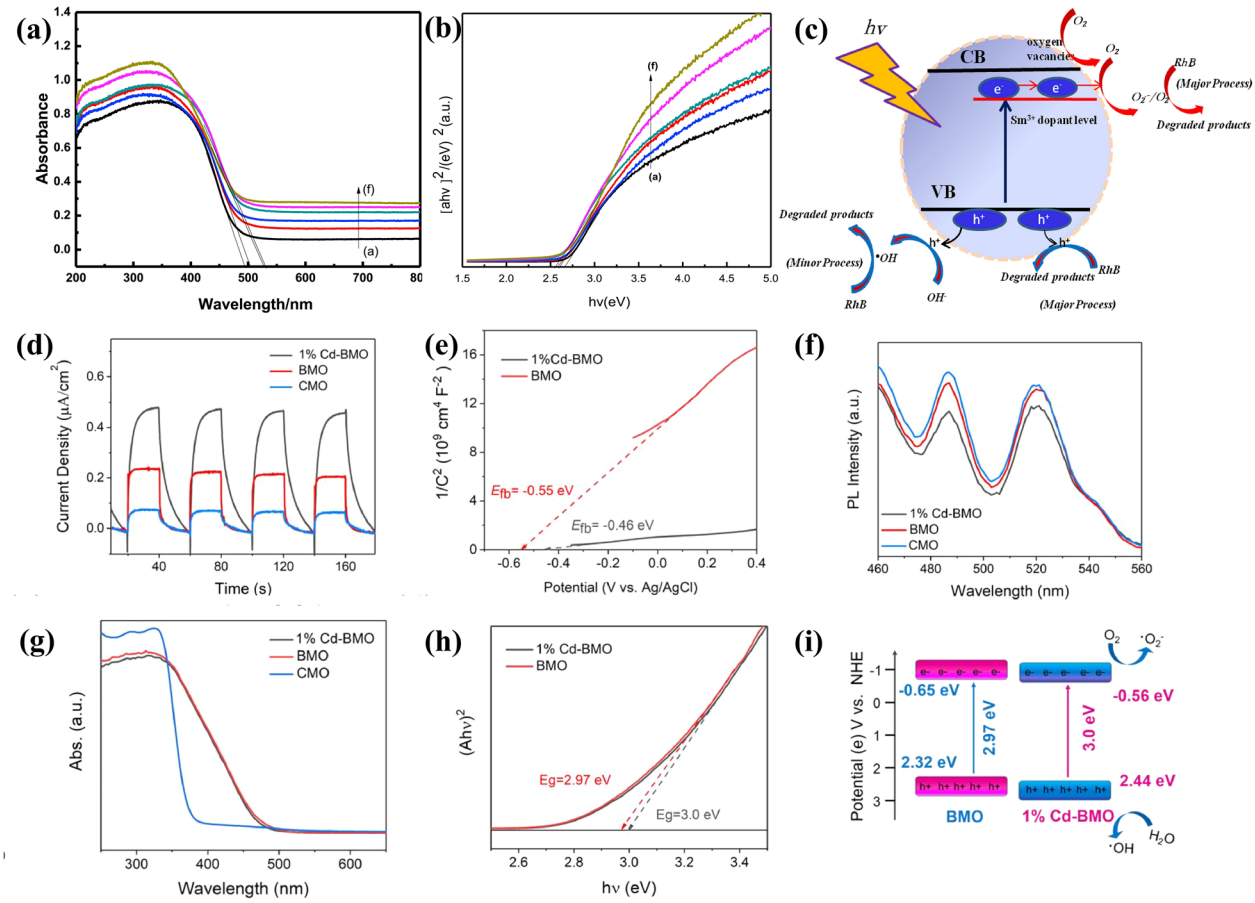

Fig. 12 UV-Vis DRS spectra of (a) Bi_2MoO_6, (b) 0.4Sm–Bi_2MoO_6, (c) 0.6Sm–Bi_2MoO_6, (d) 0.8Sm–Bi_2MoO_6, (e) 1.0Sm–Bi_2MoO_6 and (f) 1.2Sm–Bi_2MoO_6. (c) Schematic illustration of the mechanism for the photocatalytic degradation of RhB on the Sm-doped Bi_2MoO_6 photocatalyst. Reproduced from ref. 82 with permission from Elsevier. Copyright 2017. (d) Transient photocurrent density, (e) Mott–Schottky (M–S) plots, (f) fluorescence spectroscopy, (g) DRS spectra of pure $CdMoO_4$, Bi_2MoO_6 and 1% Cd–Bi_2MoO_6, (h) estimated band gaps of pure Bi_2MoO_6 and 1% Cd–Bi_2MoO_6, respectively, (i) the mechanism of 1% Cd–Bi_2MoO_6 for photocatalytic degradation. Reproduced from ref. 83 with permission from Elsevier. Copyright 2021. Note: "BMO" in this figure denotes Bi_2MoO_6. "CMO" in this figure denotes $CdMoO_4$.

demonstrated that the incorporation of different rare earth elements not only influenced the morphological evolution of Bi_2MoO_6, resulting in varied structural forms, but also significantly enhanced its visible-light absorption capability.[84] Dai *et al.* demonstrated that controlled Ce doping significantly enhances the visible-light-driven photocatalytic performance of Bi_2MoO_6 through deliberate crystal structure engineering. Their work revealed a dual substitution mechanism, where Ce^{3+} replaces Bi^{3+} and Ce^{4+} substitutes for Mo^{6+}. This process induces lattice distortion and, for charge compensation, leads to the partial reduction of Mo^{6+} to Mo^{4+} and the formation of oxygen vacancies (OVs). The creation of these OVs and crystal defects serves as a pivotal micro-mechanism, effectively trapping charge carriers and markedly suppressing the recombination of photogenerated electron–hole pairs. Furthermore, the introduced Ce^{3+}/Ce^{4+} and Mo^{4+}/Mo^{6+} redox couples actively promote the generation of reactive oxygen species. This multifunctional cerium doping strategy thus proved highly effective, significantly enhancing the photocatalytic performance of Bi_2MoO_6 across diverse applications. The Ce-doped Bi_2MoO_6, particularly the 10% Ce–Bi_2MoO_6 variant, consistently surpassed pure Bi_2MoO_6, achieving complete mineralization of nerve agent simulants methyl parathion (MP) and bis(4-nitrophenyl) phosphate (b-NPP), exceptional disinfection efficiency against *S. aureus*, and high degradation rates for organic dyes (MB and RhB).[85]

3.2.2 Non-metal doping strategy. Compared with transition metal dopants, non-metallic dopants such as B, C, and F—characterized by their smaller ionic radii—are more readily incorporated into the interstitial lattice sites of Bi_2MoO_6. These small-radius elements are particularly effective at inducing lattice defects that modulate electronic properties. A notable example of non-metal doping that provides deep insight into the micro-mechanism is iodine(I)-doped Bi_2MoO_6. In this system, I^- doping induces lattice expansion and creates defect sites that serve as effective charge trapping centers, significantly reducing PL intensity and suppressing charge recombination. More profoundly, the doped iodine species establish an internal I^-/IO_3^- redox shuttle. This mechanism provides a continuous pathway for the spatial separation of charge carriers: holes are

consumed in oxidizing I^- to IO_3^-, while electrons are simultaneously consumed in reducing IO_3^- back to I^-. This sophisticated strategy moves beyond simple band structure modification and exemplifies how dopants can create specific spatial separation pathways for electrons and holes, drastically improving quantum efficiency and photocatalytic performance for antibiotic degradation and Cr(VI) reduction.[86] In addition, Chen *et al.* prepared carbon-doped Bi_2MoO_6 (C–Bi_2MoO_6) nanosheet self-assembled microspheres *via* a solvothermal calcination method. In this structure, carbon atoms replaced O^{2-} anions in the Bi_2MoO_6 lattice, resulting in thinner nanosheets, smaller microsphere sizes, and an increased specific surface area. Among the samples, the C–Bi_2MoO_6 microspheres synthesized with a C/Bi molar ratio of 4 (denoted as 4C–Bi_2MoO_6) exhibited the highest photocatalytic activity. Under simulated solar irradiation, the RhB degradation rate constant of 4C–Bi_2MoO_6 was 2.26 times higher than that of undoped Bi_2MoO_6, demonstrating a significant enhancement in photocatalytic performance.[87]

3.2.3 Co-doping strategy. Building upon single-element doping, the co-doping strategy aims to construct a synergistic catalytic system by introducing multiple functional components to comprehensively enhance photocatalytic performance. This approach typically involves co-doping between rare-earth ions or combinations of rare-earth ions with metallic/non-metallic elements. Through rational design, these components can introduce defects into the semiconductor, modulate the band structure, broaden the light response range, and establish efficient spatial separation pathways for charge carriers, thereby achieving in-depth optimization of the photocatalytic process.

For example, a study successfully synthesized Er^{3+}/Yb^{3+} co-doped Bi_2MoO_6 flower-like microspheres with a metallic Bi core–shell structure (Bi_2MoO_6: Er^{3+}/Yb^{3+}@Bi) *via* a hydrothermal method. Under visible light irradiation, the optimized sample (Bi_2MoO_6: $Er^{3+}/0.03Yb^{3+}@Bi_{0.10}$) exhibited significantly enhanced photocatalytic activity, with a degradation rate constant of 0.0918 min^{-1}, substantially superior to that of unmodified Bi_2MoO_6 (0.0660 min^{-1}). Mechanistic studies demonstrated that the enhanced photocatalytic performance stemmed not only from improved charge separation but also from critical micro-mechanisms. Oxygen vacancies, confirmed by XPS, served as electron traps that suppressed carrier recombination while broadening light absorption and promoting O_2 activation for enhanced $^{\bullet}O_2^-$ generation. Simultaneously, metallic Bi's SPR effect created localized electromagnetic fields that facilitated electron transfer from Bi_2MoO_6 to Bi surfaces, achieving spatial charge separation. The introduced Er^{3+}/Yb^{3+} impurity levels further optimized charge transfer pathways as electron relays. Additionally, trapping experiments and ESR tests verified the crucial roles of $^{\bullet}O_2^-$, $^{\bullet}OH$, and h^+ in the degradation process.[88]

Ion doping improves light absorption and carrier mobility by altering the band structure or creating defects; however, it also presents challenges such as doping uniformity and the risk of forming recombination centers. Notably, differences in dopant ionic radii hinder precise control over photocatalytic properties, since concentration gradients and the doping mode (substitutional *versus* interstitial) often lead to uneven defect distribution within the material.

3.3. Surface topography control

The properties of a catalytic material depend not only on its chemical composition but also significantly on its structure and morphology. Photocatalysts with a larger specific surface area exhibit markedly enhanced photocatalytic performance. This is because a greater surface area provides more active sites for reactions, while smaller particle sizes can promote more efficient separation of photogenerated charge carriers.[89] Therefore, controlling the morphology offers remarkable flexibility to enhance the photocatalytic performance of photocatalysts. Bi_2MoO_6 nanostructures come in various forms, including one-dimensional nanorods, strips, tubes, and fibers; two-dimensional films, nanoplates, and sheets; as well as three-dimensional hierarchical architectures. Generally, hollow microspheres and layered structures demonstrate higher visible light utilization compared to bulk materials, leading to improved photocatalytic efficiency.

Zhang *et al.* discovered that by adjusting the pH of the reaction system, Bi_2MoO_6 nanomaterials with different morphologies—such as nanosheets and microrods—can be selectively synthesized. Notably, Bi_2MoO_6 prepared under acidic conditions showed photocatalytic activity under visible light that was 12 times higher than that of samples synthesized under alkaline conditions.[90] Zhu *et al.* synthesized Bi_2MoO_6 samples with three-dimensional microsphere morphologies *via* a hydrothermal method, varying the Bi : Mo molar ratios. Among the tested compositions, the Bi : Mo ratio of 2 : 1 exhibited the highest catalytic activity, achieving 99.43% removal of Orange II dye within 120 minutes. The microspheres' surfaces were composed of irregular nanosheets that provided abundant exposed reactive sites, significantly enhancing the degradation efficiency of Orange II.[91] Cheng *et al.* prepared a flower-like microsphere-shaped hydrothermal Bi_2MoO_6 (HT-Bi_2MoO_6) catalyst. This catalyst can effectively convert mechanical energy into electrical energy through vibration, enabling efficient degradation of dyes.[92] Dong *et al.* synthesized double-layer structured Bi_2MoO_6 blossom balls *via* a simple solvothermal method and achieved controllable introduction of OVs by subsequent calcination at different temperatures. The double-layer structure enhances light absorption efficiency through increased multiple light reflections. Compared to pristine Bi_2MoO_6, the presence of OVs modulates the band structure and promotes more efficient separation and transfer of photogenerated electron–hole pairs.[93]

Three-dimensional functional structures are usually constructed by assembling low-dimensional building blocks. This approach not only prevents the serious agglomeration often seen in low-dimensional materials but also combines the unique advantages of nanoscale components with their assembled architectures. As a result, these 3D structures offer efficient photogenerated carrier transport, enhanced light-harvesting capability, and abundant surface-active sites, collectively boosting photocatalytic performance.

4. Environmental application of Bi_2MoO_6

4.1. Application of Bi_2MoO_6 to degradation of pollutants in the environment

4.1.1 Degradation of organic dyes. As a key sector of traditional manufacturing, the textile industry inevitably generates large volumes of colored wastewater containing various persistent pollutants during production. Due to their poor biodegradability, these dyes and pigments adversely impact aquatic ecosystems by causing eutrophication, oxygen depletion, discoloration, increased turbidity, and unpleasant odors. Moreover, they pose long-term risks through persistence in the environment, bioaccumulation of carcinogenic aromatic compounds, formation of harmful chlorinated byproducts, and potential mutagenic and carcinogenic effects.[94] Textile printing and dyeing wastewater is characterized by large volumes, high concentrations of organic pollutants, strong alkalinity, significant fluctuations in water quality, and a high risk of cross-contamination. To tackle these challenges, Bi_2MoO_6 and its composites have gained attention as promising materials, thanks to their outstanding ability to degrade organic dyes effectively.

Bi_2MoO_6/TiO_2 showed rapid photodegradation of RhB under simulated sunlight (degradation rate of 91.4% in 180 min).[95] Cui *et al.* prepared an In_2S_3/Bi_2MoO_6 heterostructured photocatalyst *via* a hydrothermal method. Its degradation rate constant was 2.48 times and 6.51 times higher than those of pure In_2S_3 and Bi_2MoO_6, respectively. Additionally, the removal efficiency remained above 81.4% after multiple reuse cycles, demonstrating good stability.[96] The degradation efficiency of RhB by Ag@p-g–C_3N_4–Bi_2MoO_6 nanocomposites was 99.7%.[97]

5.0 mol% Te-doped Bi_2MoO_6 can degrade 99.7% RhB within 1 hour under visible light, 6.4 times higher than the rate constant of the original Bi_2MoO_6.[98] Similarly, Wu *et al.* developed fluorinated Bi_2MoO_6 nanocrystals *via* a solvothermal-calcination method. The incorporation of F^- ions induced lattice shrinkage, reduced crystal size, and facilitated the separation of photogenerated electron–hole pairs. The optimized $F_{0.20}$-Bi_2MoO_6 sample demonstrated a 78% removal of RhB under simulated sunlight, with a rate constant 3.5 times greater than that of undoped Bi_2MoO_6. This improvement was attributed to the synergistic effects of OVs, surface-adsorbed F^-, and a more positive VB potential, which collectively enhanced the oxidation capacity of the catalyst.[99] The synthesized Bi_2WO_6/Bi_2MoO_6 microspheres possess a high specific surface area of 12.16 $m^2\ g^{-1}$, which contributes to their enhanced solar energy harvesting and photoconversion capabilities. Consequently, the hybrid photocatalyst achieved notable photocatalytic rate constants of 0.0165 min^{-1} for RhB and 0.0378 min^{-1} for MB, respectively.[100] γ-Bi_2MoO_6 nanoparticles can effectively degrade about 93.4% of the MB dye.[101] The 2.4% MoS_2/CdS/Bi_2MoO_6-2.0 composite prepared by Wang *et al.* showed good photocatalytic activity, and the removal rate of MB within 120 min was 96.0%. In addition, the cyclic experiments show that 2.4% MoS_2/CdS/Bi_2MoO_6-2.0 has good stability and recyclability.[102]

4.1.2 Degradation of antibiotics. With the rapid progress of agriculture and industrialization, water resources face unprecedented challenges, leading to a significantly accelerated deterioration of water quality. Unabsorbed antibiotics enter the aquatic environment, exacerbating water pollution and contributing to eutrophication. Moreover, residual antibiotics in water can disrupt human microbiota, weaken immune defenses, and accelerate the development of antibiotic-resistant bacteria, posing a potential threat to human health. However, due to the high stability of antibiotics and their resistance to biological treatments, traditional methods struggle to effectively remove these contaminants. In contrast, Bi_2MoO_6 composites exhibit unique advantages in the photocatalytic degradation of antibiotics, making them an increasingly important focus of research.

The Fe_3CN/Bi_2MoO_6 catalyst achieved a TC removal rate of 95.54% within 30 minutes. Its outstanding performance is attributed to efficient Fe^{3+}/Fe^{2+} redox cycling facilitated by the decomposition of H_2O_2. Moreover, Fe_3CN/Bi_2MoO_6 demonstrates excellent photo-Fenton degradation activity across a wide pH range (3.0–11.0) and maintains good stability during TC wastewater treatment.[103] The removal rate of chlortetracycline by Bi_2MoO_6/Cu_2O composite photocatalyst was 88%.[104] The Bi_2MoO_6/g-C_3N_4 composite (1 : 32) achieved optimal sulfadiazin photodegradation under visible light, removing 93.88% within 120 min.[105] The 3D hierarchical $Bi_2MoO_6/Bi_2Sn_2O_7$ composite, synthesized *via* a solvothermal method, demonstrates significantly enhanced photocatalytic activity over its individual components. It achieves high degradation efficiencies for both RhB (95.28%) and TC (87.45%) under LED light, with excellent cycling stability.[106]

Table 1 summarizes the photocatalytic degradation efficiencies of various Bi_2MoO_6-based composites against a range of organic pollutants, including antibiotics, synthetic dyes, and other persistent contaminants. The data clearly demonstrate that Bi_2MoO_6-based photocatalysts consistently deliver high degradation efficiencies, underscoring their strong potential for environmental remediation applications. Continued research efforts focus on developing novel Bi_2MoO_6-based materials with improved photocatalytic performance, promising further advancements in pollutant removal capabilities.

4.2. Application of Bi_2MoO_6 in antibacterial properties

Microbial and antibiotic contamination present serious threats to public health, making the development of rapid and safe antibacterial strategies crucial. Recently, heterogeneous-structured photocatalytic materials have emerged as a promising research focus for combating pathogenic microorganisms. Their advantages include efficient charge separation and multi-mechanism synergistic antibacterial effects. Among these, Bi_2MoO_6-based photocatalytic materials stand out due to their excellent antibacterial performance, garnering significant attention from researchers worldwide (Table 2).

Solvothermally synthesized $AgBiO_3/Bi_2MoO_6$ heterostructures combine flower-like $AgBiO_3$ and sheet-like Bi_2MoO_6. The $AgBiO_3/Bi_2MoO_{6-10}$ variant achieved complete *E. coli*

Table 1 Comparison of degradation performance of various modified Bi_2MoO_6-based photocatalysts reported for organic pollutants

Photocatalyst	Growth method	Weight (mg)	Pollutants	Time (min)	Removal efficiency (%)	Ref.
C–Bi_2MoO_6 nanosheet self-assembled microspheres	Solvothermal-calcination method with glyoxal as the carbon source	20	100 mL RhB solution (20 mg L^{-1})	120	98.31	107
P–Bi_2MoO_6/g-C_3N_4	Solvothermal method	25	50 mL RhB solution (20 mg L^{-1})	80	99.7	108
ZnO@Bi_2MoO_6–MoS_2	One-pot hydrothermal method	30	100 mL RhB solution (20 ppm)	60	97.2	109
Self-supported Bi_2MoO_6/carbon fiber	Solvothermal method	20	50 mL RhB solution (10 mg L^{-1}) and 1.5 mmol peroxymonosulfate	80	96.8	110
CQDs (5 wt%)-Bi_2MoO_6	Hydrothermal method	30	30 mL RhB solution (5 mg L^{-1})	300	99.76	111
g-C_3N_4/BiOBr/Bi_2MoO_6	Solvothermal method	50	200 mL RhB solution (10 mg L^{-1})	180	92	112
CeO_2/Bi_2MoO_6	Precipitation and hydrothermal method	50	100 mL acid orange II solution (15 mg L^{-1})	50	85	113
Bi_2MoO_6/Corn Straw biochar	Hydrothermal method	50	100 mL BPA solution (10 mg L^{-1})	75	93	114
Bi_2MoO_6/N–TiO_2	Electrospinning method and hydrothermal synthesis	10	40 mL TCH solution (20 mg L^{-1})	90	93.76	115
Type II Bi_2MoO_6/$Bi_4O_5Br_2$ heterojunction	Two-step solvothermal method	15	30 mL TCH solution (20 mg L^{-1})	120	76	116
$Mn_{0.5}Cd_{0.5}S$/Bi_2MoO_6	Solvothermal method	30	90 mL TC solution (20 mg L^{-1})	60	90.7	117
30%-SO_{42}^{-}-Bi_2MoO_6	Solvothermal method	70	100 mL TC solution (20 mg L^{-1})	30	92.8	118
Sn–Bi_2MoO_6	Solvothermal method	20	100 mL TC solution (20 mg L^{-1})	120	81.1	119
Bi_2MoO_6/g-C_3N_4/kaolinite	Calcination crystallization and solvothermal method	40	50 mL TC solution (30 mg L^{-1})	300	90.8	120
$Bi_{19}Cl_3S_{27}$/Bi_2MoO_6	Hydrothermal method	20	80 mL TC solution (20 mg L^{-1})	75	76.58	121
$CuFe_2O_4$/Bi_2MoO_6	Solvothermal method	30	50 mL TC solution (50 mg L^{-1})	30	98.54	122
g-C_3N_4/BiOBr/Bi_2MoO_6	Solvothermal method	50	200 mL CIP solution (10 mg L^{-1})	180	94	112
Bi_2MoO_6–Br	Solvothermal method	20	50 mL sulfamethazine solution (10 mg L^{-1})	150	70	123
Bi_2MoO_6/g-C_3N_4/kaolinite	Calcination crystallization and solvothermal method	750	125 L gaseous formaldehyde (10 ppm)	180	55.5	120
Bi self-doped Bi_2MoO_6	Hydrothermal method	25	25 mL perfluorooctanoic acid solution (100 mg L^{-1})	40	88.1	124
Sn–Bi_2MoO_6	Solvothermal method	10	2-Mercaptobenzothiazole (10 mg L^{-1})	120	85.1	119

eradication within 90 min under visible light.[126] Han *et al.* developed a novel Cu_2O/Bi_2MoO_6 composite photocatalyst sensitized by UiO-66. Mott–Schottky analysis (Fig. 13a–c) confirmed n-type semiconducting behavior for Cu_2O, UiO-66, and Bi_2MoO_6, with flat-band potentials of −0.33, −0.12, and −0.15 eV Ag/AgCl, respectively. Photoelectrochemical measurements revealed enhanced carrier lifetimes and multi-pathway electron transfer within the Cu_2O/UiO-66/Bi_2MoO_6 ternary system, attributed to UiO-66-mediated photocorrosion suppression and efficient charge transfer from Bi_2MoO_6 to Cu_2O. Antibacterial assays against *S. aureus*, methicillin-resistant *Staphylococcus aureus* (MRSA), and *E. coli* (Fig. 13d–g) demonstrated near-complete sterilization (>99.9%) under light irradiation. Additionally, the Cu_2O/UiO-66/Bi_2MoO_6 composite exhibited superior anticancer activity against HepG2 cells compared to Flu-5.[133] The $CuBi_2O_4$/Bi_2MoO_6 p–n heterojunction exhibits enhanced visible-light (λ > 420 nm) antibacterial performance against *E. coli* compared to its individual components. Specifically, the $CuBi_2O_4$/Bi_2MoO_6-0.5 hybrid achieves complete inactivation of *Escherichia coli* cells within 4 hours. The antibacterial mechanism involves damage to the bacterial cell membrane, leading to leakage and degradation of intracellular contents, including total proteins and DNA.[134]

4.3. Performance in complex water matrices and practical application potential

Although laboratory studies have confirmed the excellent photocatalytic performance of Bi_2MoO_6 and its composites in simulated wastewater, their practical application efficacy is significantly influenced by complex water matrices. Common

Table 2 Comparison of the antibacterial activity by different modified Bi_2MoO_6-based photocatalysts

Photocatalyst	Growth method	Weight (mg)	Pollutants	Time (min)	Photocatalytic activity	Ref.
Bi_2MoO_6/Bi_5O_7I	*In situ* solvothermal method	20	50 mL *Escherichia coli* solution (108 cfu mL^{-1})	90	Completely achieve disinfection	125
$AgBiO_3/Bi_2MoO_6$	Hydrothermal method	0.05	10 mL *Escherichia coli* solution	90	Completely achieve disinfection	126
Bi_2MoO_6/Ag–AgCl	Chemical precipitation and photo-reduction	1	10 mL *Escherichia coli* solution (107 cfu mL^{-1})	30	Completely achieve disinfection	127
Bi_2MoO_6/red phosphorus heterojunction	Hydrothermal method	15	25 mL *Escherichia coli* solution (2.84 × 108 cfu mL^{-1})	30	The colony count was decreased to 1.6 × 107 cfu mL^{-1}	128
AgI/Bi_2MoO_6	Solvothermal-precipitation approach	4	50 mL *Escherichia coli* and *Staphylococcus aureus* solution (5.0 × 107 cfu mL^{-1})	30 and 90, respectively	Complete disinfection was achieved, respectively	129
MoS_2/Bi_2MoO_6	Bath evaporation method	100	100 mL *Escherichia coli* solution (106 cfu mL^{-1})	60	The survival ratio reduced to (60.3 ± 3.7)%	130
Bi_2MoO_6–AgBr	Adsorption-deposition method	6	50 mL *Escherichia coli* solution (3 × 106 cfu mL^{-1})	90	Completely achieve disinfection	131
$CuBi_2O_4/Bi_2MoO_6$	Solvothermal method	40	50 mL *Escherichia coli* solution (107 cfu mL^{-1})	240	Almost completely disinfected	132

inorganic anions and cations in real water bodies, such as Cl^-, NO_3^-, SO_4^{2-}, CO_3^{2-}/HCO_3^-, Ca^{2+}, and Mg^{2+}, can inhibit degradation by competing for photogenerated active species or altering the solution environment. The synergistic effect of cations and pH is particularly critical, as the solution pH influences both the catalyst surface charge and the speciation of the pollutant. For example, the degradation rate of TCH by CeO_2 quantum dots/Bi_2MoO_6 S-scheme heterojunction was much higher under alkaline conditions (approximately 88% at pH = 9 and 11) than under acidic conditions (approximately 52% at pH = 3 and 5). This is attributed to the more facile generation of $^{\bullet}OH$ radicals from the oxidation of OH^- by holes (h^+) in alkaline media, coupled with the transformation of TCH into the more readily degradable isotetracycline form.[135]

Natural Organic Matter (NOM), such as humic and fulvic acids, is another key factor affecting photocatalytic efficiency. The light-shielding effect of NOM was demonstrated during the degradation experiments with a PDI/Bi_2MoO_6 composite in Wei River water, where the persistent fluorescence peak of humic acid-like organics after reaction indicated competition with the catalyst for photon absorption.[136] Furthermore, NOM acts as a high-concentration background organic substance that scavenges photogenerated holes and radicals, leading to reduced degradation efficiency for target pollutants like CIP. The complex and high organic load of actual wastewater poses a more severe challenge, resulting in a comprehensive inhibitory effect. Performance attenuation is commonly observed when transitioning from simulated to real wastewater. For instance, the degradation efficiency of TCH by CeO_2/Bi_2MoO_6 dropped from 91.2% in deionized water to 71.9% in pharmaceutical wastewater. Similarly, the C_3N_4/Bi_2MoO_6/carbon fiber cloth achieved an 86% degradation of TC under optimal acidic conditions (pH = 5), a performance that surpasses its individual components. While the presence of common coexisting ions had an insignificant impact on TC degradation, a slight but consistent performance decline was observed when moving from deionized water (86%) to tap water (83%) and lake water (81%), highlighting the subtle yet tangible effect of complex background substances.[137] This trend of varying efficiency across different water sources is further exemplified by the N, S-GQDs and Au co-modified Bi_2MoO_6, which exhibited high and stable degradation efficiency for oxytetracycline in tap water (80.15%), lake water (78.36%), and river water (79.16%). Notably, a more discernible efficiency reduction was observed in industrial wastewater (76.31%) and medical wastewater (75.32%), clearly illustrating a performance gradient that correlates with the increasing complexity and organic load of the water matrix.[138]

In summary, the transition from simulated to real wastewater universally leads to a measurable attenuation in the performance of Bi_2MoO_6-based photocatalysts, establishing a clear inverse correlation between catalytic efficiency and the complexity of the water matrix. Nevertheless, the evidence presented herein confirms that this performance gap can be significantly bridged through rational material design, underscoring the necessity of evaluating and developing these advanced materials under environmentally relevant conditions.

5. Emerging applications in energy conversion and storage

The escalating global energy demand and the urgent need to mitigate climate change have spurred extensive research into sustainable and clean energy technologies. Photocatalysis, which directly converts solar energy into chemical fuels, stands at the forefront of these efforts.[139] Among the various photocatalytic materials, Bi_2MoO_6 has emerged as a particularly versatile visible-light-responsive photocatalyst. Its tunable band

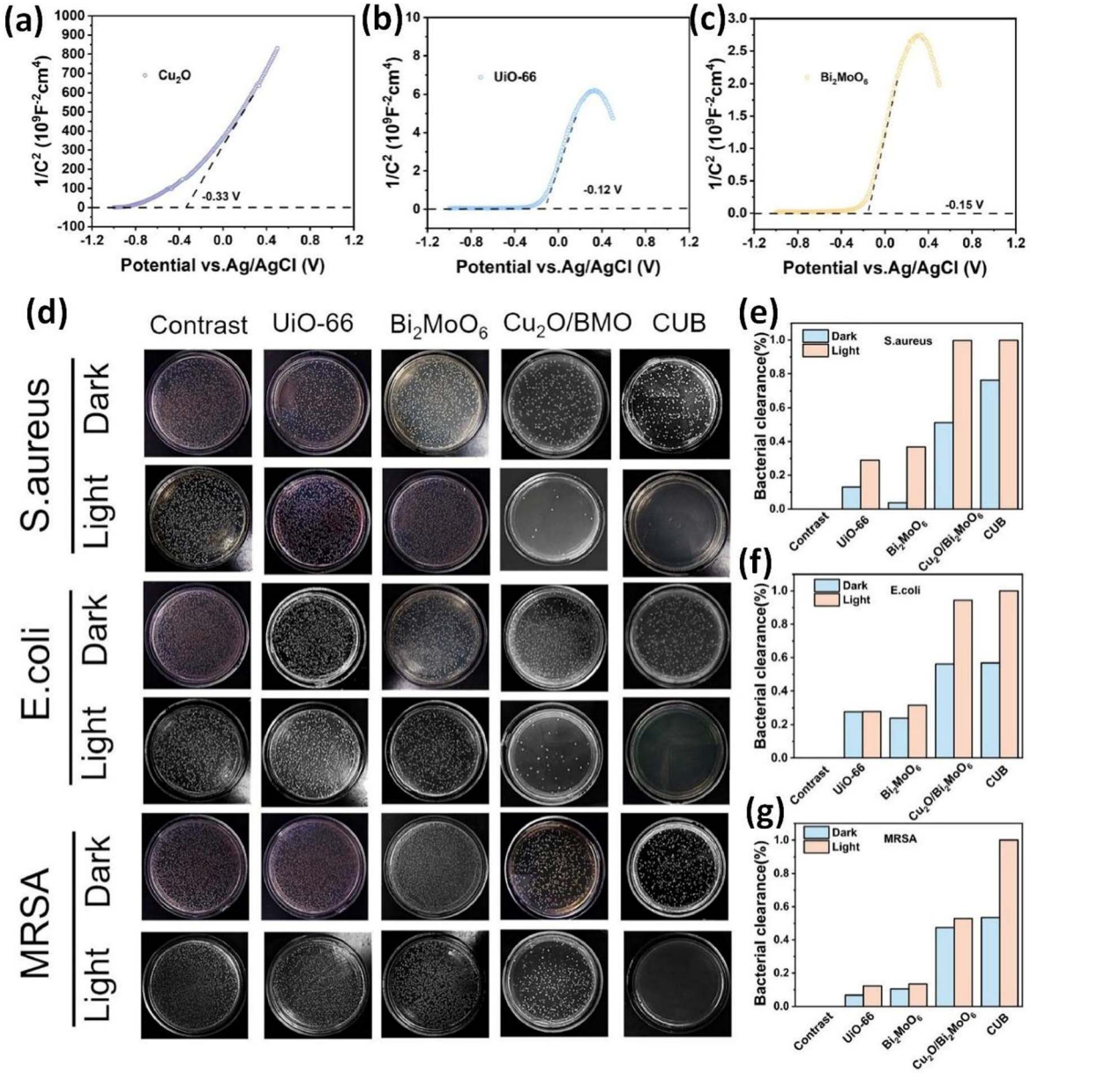

Fig. 13 (a–c) Mott's Schottky plots of Cu_2O, UiO-66, and Bi_2MoO_6; (d) the bacteriostatic effect of UiO-66, Bi_2MoO_6, Cu_2O/Bi_2MoO_6, and CUB treatments on *Staphylococcus aureus*, *Escherichia coli*, and MRSA; (e–g) Histogram of the bacteriostatic effect of each material against several bacteria. Reproduced from ref. 133 with permission from Elsevier. Copyright 2025.

structure, layered architecture, and chemical stability make it a promising candidate for a trio of critical energy conversion reactions: hydrogen evolution, carbon dioxide reduction, and nitrogen fixation. While each reaction faces distinct challenges—such as the inertness of CO_2 and N_2 molecules or the competing hydrogen evolution reaction (HER)—a common strategy to enhance the performance of Bi_2MoO_6 lies in the rational design of composite structures. By constructing sophisticated heterojunctions (*e.g.*, S-scheme, Z-scheme) and introducing defect engineering, researchers can effectively modulate the charge separation dynamics and surface reaction pathways of Bi_2MoO_6-based catalysts.

5.1. Photocatalytic hydrogen evolution

The relentless consumption of fossil fuels has precipitated a dual crisis of energy scarcity and environmental degradation, driving the urgent quest for sustainable alternatives.[139] Hydrogen, with its high energy density and zero-carbon emissions upon combustion, is widely regarded as the ultimate clean energy carrier. Photocatalytic water splitting, which harnesses solar energy to directly extract hydrogen from water, represents a paradigm shift towards renewable hydrogen production. Among various photocatalysts, Bi_2MoO_6 has emerged as a promising visible-light-driven candidate for the HER.[140,141] Its intrinsic advantages, including a suitable CB position for

proton reduction and a narrow bandgap for visible-light absorption, are nonetheless hampered by rapid charge carrier recombination. To unlock its full potential, the construction of advanced heterojunctions—such as S-scheme, 3D/2D, and ternary composites—has proven to be a highly effective strategy. These engineered interfaces are pivotal for directing charge flow and suppressing recombination, thereby translating the promise of solar hydrogen into dramatically enhanced production rates.

Additionally, a separate system featuring a 2D/2D S-scheme heterojunction composed of Bi_2MoO_6 and an ultra-thin Zn-based metal–organic framework using tetrakis(4-carboxyphenyl) porphyrin (Zn-TCPP) as the ligand. The extensive interfacial contact between the two 2D components, together with the built-in electric field and coulombic attraction inherent to the S-scheme mechanism, promotes directed carrier migration. The resulting Bi_2MoO_6/Zn-TCPP composite achieves a hydrogen evolution rate of 10900.94 μmol g^{-1} h^{-1}, surpassing pure Bi_2MoO_6 and Zn-TCPP by factors of 38.9 and 3.24, respectively.[142]

Beyond hydrogen evolution, Bi_2MoO_6-based systems also enable overall water splitting without sacrificial agents. A 3D/2D hybrid of $SrTiO_3$ nanocubes and Bi_2MoO_6 nanoflakes exemplifies this capacity. In this system, $SrTiO_3$ primarily facilitates the HER, while Bi_2MoO_6, with its more positive VB potential, excels in the oxygen evolution reaction (OER). The optimal sample, with a $SrTiO_3$ content of 50 wt%, demonstrated the highest photocatalytic activity and stability. The close interfacial contact ensures efficient intercomponent charge transfer, yielding H_2 and O_2 evolution amounts of 3350 μmol g^{-1} and 1875 μmol g^{-1} over 8 hours, with stable performance over multiple cycles.[143] Researchers have designed a Bi_2MoO_6/g-C_3N_4/multi-walled carbon nanotube (CNT) ternary nanocomposite to produce hydrogen fuel from water using simulated solar energy. Here, CNTs serve as an electron conduit and form a pseudo-Schottky junction, effectively extracting and shuttling photogenerated electrons from the Bi_2MoO_6/g-C_3N_4 interface. This system attains a hydrogen evolution amount of 3480 μmol g^{-1}, substantially exceeding that of the binary Bi_2MoO_6/g-C_3N_4 composite (1980 μmol g^{-1}) and its individual constituents.[144]

5.2. Photocatalytic CO_2 reduction

The excessive emission of CO_2 from fossil fuel combustion is the primary culprit behind global warming and climate change. Photocatalytic CO_2 reduction offers a transformative "kill two birds with one stone" strategy, simultaneously addressing both the energy crisis and environmental issues by converting the greenhouse gas into valuable solar fuels, such as CO and CH_4.[145–147] This artificial photosynthetic process aims to close the carbon cycle, storing intermittent solar energy in the chemical bonds of portable fuels. The key challenges, however, lie in the extreme chemical inertness of the CO_2 molecule and the complexity of its multi-electron reduction pathways. Bi_2MoO_6-based materials, with their moderate CB potential and highly tunable surface properties, show immense promise in this field. Their true potential is realized when engineered into sophisticated heterostructures, particularly S-scheme and Z-scheme heterojunctions. These designs are crucial not only for achieving efficient spatial charge separation but, more importantly, for preserving the strong redox potentials necessary to drive the challenging CO_2 reduction reactions with high selectivity.

A breakthrough was achieved by constructing a hierarchical S-scheme heterojunction between Bi_2MoO_6 nanoflakes rich in surface oxygen vacancies (SOVs) and In_2S_3 nanotubes (Bi_2MoO_6-SOVs@In_2S_3). This design synergized multiple advantages: the hollow tubular structure enhanced light harvesting, while the SOVs served as highly active centers for CO_2 adsorption and activation. The S-scheme mechanism ensured efficient charge separation, resulting in an exceptional CO-production rate of 28.54 μmol g^{-1} h^{-1} under visible light and high CO selectivity (~94.1%).[148] In another exemplary study, a 2D/2D van der Waals heterojunction was constructed by coupling few-layered Bi_2MoO_6 nanosheets with BiOI nanosheets. This architecture created a large-area, intimate interface conducive to rapid charge transfer *via* an S-scheme pathway. This mechanism effectively preserved the strong reduction ability of BiOI for CO_2 reduction, leading to production rates of 8.34 μmol g^{-1} h^{-1} for CO and 3.31 μmol g^{-1} h^{-1} for CH_4.[149]

Notably, the charge transfer pathway is not limited to the S-scheme. The construction of a Z-scheme heterojunction can also yield exceptional performance. Jiao *et al.* constructed a 2D/2D Z-scheme heterojunction between S-doped graphitic carbon nitride (SCN) and Bi_2MoO_6. The S-doping effectively narrowed the band gap of g-C_3N_4 and served as active sites, while the microwave-assisted synthesis created an intimate interfacial connection. The Z-scheme mechanism directed the transfer of photogenerated electrons from the CB of Bi_2MoO_6 to the VB of SCN, thereby preserving the most powerful holes in Bi_2MoO_6 and the most powerful electrons in SCN for redox reactions. This system exhibited a remarkable selectivity of 99.15% for converting CO_2 to CH_3OH, with a production rate of 6.19 μmol g^{-1} h^{-1}, and maintained 94.6% of its initial activity after six cycles.[150]

5.3. Photocatalytic nitrogen fixation

Nitrogen is fundamental to life and modern agriculture, yet the industrial production of NH_3 *via* the century-old Haber–Bosch process is exceptionally energy-intensive, consuming ~2% of the world's annual energy supply and contributing significantly to global carbon emissions.[151] Photocatalytic nitrogen fixation, which leverages solar energy to convert atmospheric N_2 into NH_3 under ambient conditions, presents a revolutionary and sustainable alternative. This process mimics nature's nitrogen cycle but faces the monumental challenge of activating the ultra-stable N≡N triple bond.[152,153] Bi_2MoO_6-based materials have recently garnered attention as promising catalysts for this demanding reaction. The focus of research has shifted from mere charge separation to the precise engineering of surface active sites. Key strategies, such as the creation of OVs and strategic anion doping, are employed to tailor the local

electronic structure of Bi_2MoO_6. These defects serve as exclusive hubs for N_2 adsorption and activation, effectively suppressing the competing HER and steering the photocatalytic process towards efficient ammonia synthesis.

A notable example is the construction of a Bi_2MoO_6/bismuth-based metal–organic framework (Bi_2MoO_6/Bi-MOF) composite, where the concentration of surface OVs in the Bi-MOF component was meticulously controlled. The porous Bi-MOF provided a high specific surface area for N_2 enrichment, while the OVs served dual functions: acting as trapping sites for photogenerated electrons to suppress charge recombination, and providing active centers for N_2 adsorption and activation. The internal electric field at the Bi_2MoO_6/Bi-MOF interface facilitated the flow of electrons from Bi_2MoO_6 to the OVs in Bi-MOF, where they were utilized for N_2 reduction. The optimized catalyst achieved an outstanding NH_3 production rate of 125.78 μmol g^{-1} h^{-1}, which was 21.4 times and 3.7 times higher than that of pristine Bi_2MoO_6 and the OV-free composite, respectively.[154] Liu *et al.* discovered that doping S^{2-} ions into the Bi_2MoO_6 lattice (S–Bi_2MoO_6) could significantly boost its photocatalytic nitrogen fixation performance. Even with an extremely low doping content, the S atoms, which preferentially substituted lattice O^{2-}, induced a notable upward shift of the CB minimum, endowing S–Bi_2MoO_6 with a more negative reduction potential (−0.72 V *vs.*.HNE) crucial for N_2 reduction. Furthermore, the S-doping created a defect level near the CB, which enhanced visible light absorption and served as an electron acceptor to suppress charge recombination. As a result, the optimized 0.7% S–Bi_2MoO_6 catalyst achieved a high NH_3 production rate of 122.14 μmol g^{-1} h^{-1}, which was 3.67 times that of the pristine Bi_2MoO_6. Importantly, the study confirmed through Nitrogen temperature-programmed desorption (N2-TPD) and control experiments that the enhancement primarily stemmed from improved charge separation and increased reduction capability, rather than a change in oxygen vacancy concentration, and that the competing HER was effectively suppressed.[155]

6. Conclusion and prospect

Bi_2MoO_6-based photocatalysts have demonstrated significant potential in the field of environmental remediation, owing to their tunable bandgap, non-toxic nature, structural stability, and facile synthesis. This review systematically outlined the recent advancements in modification strategies for enhancing the photocatalytic activity of Bi_2MoO_6, including heterojunction construction, ion doping, and surface topography control. These approaches have been shown to effectively promote charge separation, expand visible-light absorption, and improve overall photocatalytic efficiency.

Z-Scheme and S-scheme heterojunctions have emerged as particularly effective configurations, enabling efficient electron–hole separation while preserving the strong redox potential of charge carriers. Similarly, OVs play a vital role in introducing defect levels that enhance visible light absorption and create active catalytic sites; however, their controllability remains limited. Elemental doping, especially with rare-earth and precious metals, can significantly modify surface area and electronic structure, although cost and scalability remain major concerns. Furthermore, advanced strategies such as the anchoring of single atoms *via* surface vacancies, as well as leveraging specific crystal planes to guide charge transfer, show promise but are technically challenging due to the structural complexity of Bi_2MoO_6.

The efficacy of these optimized Bi_2MoO_6 materials has been rigorously demonstrated in two primary domains. In environmental remediation, they exhibit outstanding performance in the degradation of prevalent pollutants, including organic dyes and antibiotics. More importantly, their inherent biocompatibility and light-induced reactive oxygen species generation empower them with robust antibacterial properties, opening avenues for water disinfection and antibacterial surfaces. In the realm of energy conversion and storage, Bi_2MoO_6-based composites have proven to be highly versatile, driving key reactions such as photocatalytic hydrogen evolution, CO_2 reduction to solar fuels, and nitrogen fixation under ambient conditions. The construction of specific heterojunctions (*e.g.*, S-scheme) is crucial here, not only for charge separation but for preserving the high redox potentials required for these challenging multi-electron processes.

Despite these advances, several critical challenges hinder the large-scale practical application of Bi_2MoO_6-based photocatalysts.

(1) From a methodological perspective, current synthesis routes for these advanced materials are often time-consuming, complex, and prone to introducing impurities. Hence, innovative and simplified preparation methods are required.

(2) On the application side, while the scope has expanded from pollutant degradation to antibacterial action and energy production, most studies remain limited to liquid-phase systems and laboratory-scale experiments. A paramount challenge for real-world environmental applications, particularly in complex wastewater matrices, lies in performance attenuation. The presence of coexisting ions (*e.g.*, Cl^-, CO_3^{2-}), natural organic matter, and fluctuating pH levels can significantly suppress degradation efficiency and antibacterial efficacy through competitive consumption of reactive species and light-shielding effects. Similarly, in energy applications, competing reactions (especially the hydrogen evolution reaction in nitrogen fixation) and the low concentration of target gas reactants (CO_2, N_2) in aqueous environments pose significant barriers to efficiency and selectivity. Their application in gas-phase and solid-phase pollutant removal warrants further exploration.

(3) Looking forward, future research should prioritize the integration of Bi_2MoO_6's intrinsic properties—such as piezoelectricity, ferroelectricity, and magnetism—with external auxiliary energy fields (*e.g.*, photo-Fenton, electrocatalysis, piezocatalysis) to further expand the functional scope of Bi_2MoO_6-based systems and create synergistic effects that overcome current limitations in both environmental and energy catalysis.

(4) Additionally, mechanistic investigations combining thermodynamic analysis, energy band alignment, and theoretical modeling will be essential to unravel the underlying

principles governing the diverse photocatalytic processes. To achieve industrial viability, research efforts must also focus on developing recyclable catalyst supports and scalable production techniques. Crucially, future work must address the practical challenges of catalyst recovery and long-term stability in continuous-flow systems, for both water treatment and gas-phase reactors. It is also imperative to evaluate the ecological safety of intermediate products formed during the degradation process in complex aqueous environments and to assess the potential leaching of metal components from the catalysts.

In conclusion, while Bi_2MoO_6-based photocatalysts have made considerable progress, evolving from a material for simple pollutant degradation to a versatile platform for integrated environmental and energy applications, continued interdisciplinary research is imperative to overcome existing limitations and realize their full potential in sustainable technologies.

Author contributions

Yiying Li: conceptualization, writing – original draft. Jingmei Li: conceptualization, supervision. Zhilin Li: data curation, writing – review & editing. Enxiang Bi: data curation, writing – review & editing.

Conflicts of interest

The authors declare no conflict of interest.

Data availability

Data availability is not applicable to this article as no new data were created or analyzed in this study.

Acknowledgements

Thanks to the support of Development and Reform Commission of Jilin Province, China (2022C039-5), Department of Education of Jilin Province, China (2020285I1IC002Y), Science and Technology Research Project of Jilin Provincial Department of Education, China (JJKH20231430KJ), Jilin Province Higher Education Research Topic (JGJX2023C27).

References

1 Z. Liu, Y. H. Gan, J. Luo, X. Luo, C. C. Ding and Y. B. Cui, *Water*, 2025, **17**, 85.
2 M. Ahmaruzzaman, S. R. Mishra, V. Gadore, G. Yadav, S. Roy, B. Bhattacharjee, A. Bhuyan, B. Hazarika, J. Darabdhara and K. Kumari, *J. Environ. Chem. Eng.*, 2024, **12**, 112964.
3 M. Gavrilescu, *Water*, 2021, **13**, 2746.
4 M. Xiao, B. Luo, S. C. Wang and L. Z. Wang, *J. Energy Chem.*, 2018, **27**, 1111–1123.
5 X. L. Song, L. Chen, L. J. Gao, J. T. Ren and Z. Y. Yuan, *Green Energy Environ.*, 2024, **9**, 166–197.
6 F. Q. Zhan, G. C. Wen, R. X. Li, C. C. Feng, Y. S. Liu, Y. Liu, M. Zhu, Y. H. Zheng, Y. C. Zhao and P. La, *Phys. Chem. Chem. Phys.*, 2024, **26**, 11182–11207.
7 B. Anusha, M. Anbuchezhiyan, R. Sribalan and N. S. A. Arunsankar, *Appl. Phys. A:Mater. Sci. Process.*, 2022, **128**, 411.
8 H. N. Zhang, L. H. Tian, Z. Q. Zhang, J. P. Han, Z. G. Wu, Z. Q. Wei, S. F. Wang, Y. Cao, S. Zhang and Y. Zhang, *Surf. Interfaces*, 2024, **55**, 105315.
9 H. J. Li, Y. T. Yao, X. Y. Yang, X. S. Zhou, R. Lei and S. F. He, *Environ. Sci. Pollut. Res.*, 2022, **29**, 68293–68305.
10 S. Galeas, V. H. Guerrero, P. I. Pontón, C. S. Valdivieso-Ramírez, P. Vargas-Jentzsch, P. Zarate and V. Goetz, *Molecules*, 2024, **29**, 3690.
11 Y. J. O. Asencios, V. S. Lourenço and W. A. Carvalho, *Catal. Today*, 2022, **388**, 247–258.
12 S. A. B. Gilani, F. Naseeb, A. Kiran, M. U. Ihsan, J. Iqbal, H. M. A. Javed, H. N. Bhatti, A. M. Karami, S. Hussain and M. Shabirmahr, *Opt. Mater.*, 2024, **148**, 114871.
13 Y. N. Han, X. W. Chen, M. Tinoco, S. Fernández-Garcia, A. B. Hungría, Y. X. Li, J. Y. Nai, R. A. Wu, A. Aguinaco, E. Blanco, J. J. Calvino and L. Jiang, *Appl. Surf. Sci.*, 2024, **678**, 161072.
14 L. Lv, Y. F. Li, J. Tang and F. X. Zhang, *Opt. Mater.*, 2025, **159**, 116600.
15 X. F. Sun, J. Q. Zhang, J. Y. Ma, T. Xian, G. R. Liu and H. Yang, *Chem. Eng. J.*, 2024, **496**, 153961.
16 L. H. Jian, G. W. Wang, X. H. Liu and H. C. Ma, *Escience*, 2024, **4**, 100206.
17 C. C. Chu, Z. Chen, D. C. Yao, X. R. Liu, M. J. Cai and S. Mao, *Angew. Chem., Int. Ed.*, 2024, **63**, e202317214.
18 F. H. Wang, Q. Zhao, H. P. Li, Q. S. Wu, L. Y. Zhang, Y. Li, L. Qiao, Y. Yuan, J. Ma, P. P. Wang and T. M. Chen, *Chem. Eng. J.*, 2024, **481**, 148855.
19 F. Stelo, N. Kublik, S. Ullah and H. Wender, *J. Alloys Compd.*, 2020, **829**, 154591.
20 J. H. Zhao, H. Q. Wang, Y. H. Cai, J. J. Zhao, Z. D. Gao and Y. Y. Song, *ACS Sens.*, 2024, **9**, 1644–1655.
21 B. L. Zhang, B. Sun, F. X. Liu, T. T. Gao and G. W. Zhou, *Sci. China Mater.*, 2024, **67**, 424–443.
22 X. Tang, A. W. Yu, Q. Q. Yang, H. Y. Yuan, Z. H. Wang, J. Z. Xie, L. H. Zhou, Y. Guo, D. Ma and S. Dai, *J. Am. Chem. Soc.*, 2024, **146**, 3764–3772.
23 C. Song, L. Q. Xiao, Y. Chen, F. Yang, H. Y. Meng, W. Y. Zhang, Y. F. Zhang and Y. Wu, *Catalysts*, 2024, **14**, 366.
24 M. A. Ahmed, S. A. Mahmoud and A. A. Mohamed, *RSC Adv.*, 2024, **14**, 25629–25662.
25 X. H. Wu, L. H. Tan, G. Q. Chen, J. Y. Kang and G. H. Wang, *Sci. China Mater.*, 2024, **67**, 444–472.
26 S. Gupta and R. Kumar, *Nanoscale*, 2024, **16**, 6109–6131.
27 X. W. Zou, B. Sun, L. Wang, H. C. Bai, X. C. Meng, C. H. Li and Z. Z. Li, *Chem. Eng. J.*, 2024, **482**, 148818.
28 H. K. Yang, Z. C. Zhang, J. Li, L. Song and B. Wang, *Chem. Eng. J.*, 2024, **487**, 150554.

29 H. B. Yu, L. B. Jiang, H. Wang, B. B. Huang, X. Z. Yuan, J. H. Huang, J. Zhang and G. M. Zeng, *Small*, 2019, **15**, 1901008.
30 S. B. Cao, J. Li, L. Wu, X. Q. Mao, S. J. Zou, Y. Li, K. Da, J. Yang and X. M. Fan, *J. Mol. Struct.*, 2024, **1317**, 139137.
31 H. H. Wang, X. S. Li, D. Yang, C. X. Chen, Y. H. Duan, J. Wang and W. Y. Guo, *Appl. Surf. Sci.*, 2025, **687**, 162246.
32 Y. H. Wu, M. T. Shen, M. Zhou, H. Li, Q. Liang, Y. N. Wang, S. Xu and Z. Y. Li, *Chem. Eng. J.*, 2025, **505**, 159174.
33 Y. Z. Chen, L. S. Wu, L. W. Liang, D. Liu, J. J. Luo, Q. F. Lv, L. L. Liang and H. T. Deng, *J. Alloys Compd.*, 2024, **1008**, 176682.
34 Y. F. Li, H. L. Wang, J. Y. Liu, X. D. Liu, J. Guan, J. C. Fu and S. J. Li, *Environ. Res.*, 2024, **263**, 120212.
35 W. F. Guo, H. P. Li, H. S. Ma and W. X. Teng, *J. Chem.*, 2014, **2014**, 436485.
36 H. Y. You, S. A. Liu, N. Ta, Y. Li and W. J. Shen, *Catal. Sci. Technol.*, 2024, **14**, 2259–2267.
37 Y. N. Zhu, J. J. Mu, G. H. Zheng, Z. X. Dai, L. Y. Zhang, Y. Q. Ma and D. W. Zhang, *Ceram. Int.*, 2016, **42**, 17347–17356.
38 J. Q. Xue, F. Li, S. H. Li, J. Zhang and Q. Bi, *Int. J. Electrochem. Sci.*, 2022, **17**, 220136.
39 W. Guo, H. Li, H. Ma and W. Teng, *J. Chem.*, 2014, **2014**, 436485.
40 Y. Wei, J. Wang, J. Ma, F. Kong, J. Xue, Z. Ye, S. Ma and S. Zhao, *Sep. Purif. Technol.*, 2024, **349**, 127860.
41 H. Huang, L. Liu, Y. Zhang and N. Tian, *J. Alloys Compd.*, 2015, **619**, 807–811.
42 Z. X. Yang, M. Shen, K. Dai, X. H. Zhang and H. Chen, *Appl. Surf. Sci.*, 2018, **430**, 505–514.
43 H. Wang, W. D. Zhang, X. W. Li, J. Y. Li, W. L. Cen, Q. Y. Li and F. Dong, *Appl. Catal., B*, 2018, **225**, 218–227.
44 M. Kasinathan, S. Thiripuranthagan, A. Sivakumar, S. Ranganathan, T. Vembuli, S. Kumaravel and E. Erusappan, *Mater. Res. Bull.*, 2020, **125**, 110782.
45 T. Chankhanittha, V. Somaudon, J. Watcharakitti, V. Piyavarakorn and S. Nanan, *Mater. Lett.*, 2020, **258**, 126764.
46 G. P. Zhang, D. Y. Chen, N. J. Li, Q. F. Xu, H. Li, J. H. He and J. M. Lu, *Appl. Catal., B*, 2019, **250**, 313–324.
47 S. C. Zhang, X. L. Li, M. Y. Huang, M. D. Shan, J. Chen, F. Q. Hao, J. M. Li, J. F. Luan, W. Zhang and F. B. Liang, *Chemistryselect*, 2022, **7**, e202200969.
48 D. X. Ji, Y. G. Lin, X. Y. Guo, B. Ramasubramanian, R. W. Wang, N. Radacsi, R. Jose, X. H. Qin and S. Ramakrishna, *Nat. Rev. Methods Primers*, 2024, **4**, 1.
49 J. Zhao, Q. Lu, C. Wang and S. Liu, *J. Nanopart. Res.*, 2015, **17**, 189.
50 K. Li, Y. Pang and Q. Lu, *Inorg. Chem. Front.*, 2019, **6**, 3215–3224.
51 J.-J. Zhang, C.-M. Kai, F.-J. Zhang and Y.-R. Wang, *Colloids Surf., A*, 2022, **648**, 129255.
52 D. Xu, F. Sun, F. Liu, H. Shao, W. He, L. Wang, Q. Ma, W. Yu, H. Yu and X. Dong, *J. Environ. Chem. Eng.*, 2024, **12**, 111952.
53 Q. Y. Wang, Q. F. Lu, M. Z. Wei, E. Y. Guo, L. B. Yao and K. Sun, *J. Sol-Gel Sci. Technol.*, 2018, **85**, 84–92.
54 J. Zhao, Z. D. Liu and Q. F. Lu, *Dyes Pigm.*, 2016, **134**, 553–561.
55 C. C. Zhao, C. L. Shao, X. H. Li, X. W. Li, R. Tao, X. J. Zhou and Y. C. Liu, *J. Alloys Compd.*, 2018, **747**, 916–925.
56 S. Jin, H. Hao, Y. Gan, W. Guo, H. Li, X. Hu, H. Hou, G. Zhang, S. Yan, W. Gao and G. Liu, *Mater. Chem. Phys.*, 2017, **199**, 107–112.
57 K. Benazir, R. Siranjeevi, R. Susmitha, S. S. Shabnum, C. K. Raj, P. Nivetha, A. Saravanan and A. S. Vickram, *J. Hazard. Mater. Adv.*, 2025, **18**, 100713.
58 J. Li, X. Liu, L. Pan, W. Qin and Z. Sun, *RSC Adv.*, 2014, **4**, 62387–62392.
59 J. Li, X. Nie, L. Meng, X. Zhang, L. Bai, D.-f. Chai, W. Zhang, Z. Zhang and G. Dong, *Appl. Surf. Sci.*, 2024, **678**, 161143.
60 J. P. Fernández-Hernán, B. Torres, A. J. López and J. Rams, *Gels*, 2022, **8**, 426.
61 D. Bokov, A. T. Jalil, S. Chupradit, W. Suksatan, M. J. Ansari, I. H. Shewael, G. H. Valiev and E. Kianfar, *Adv. Mater. Sci. Eng.*, 2021, **2021**, 5102014.
62 M. Sun, P. Guo, M. Wang and F. Ren, *Optik*, 2019, **199**, 163319.
63 P. Zhu, R. Wang, M. Duan, Y. Chen, M. Hu, X. Luo and H. Teng, *Chemistryselect*, 2019, **4**, 12022–12031.
64 D. Nguyen Trung, T. Le Minh, T. Ung Thi Dieu, T. Vu Tri, T. Nguyen Thi, T. Nguyen Thi Cam, K.-Y. A. Lin and H. Nguyen Nhat, *Environ. Sci.:Nano*, 2022, **9**, 3973–3991.
65 K. Thamaraiselvi, G. Palanisamy, P. S. M. Kumar, J. Lee and J.-J. Shim, *Chem. Eng. J.*, 2025, **511**, 161947.
66 X. Jia, S. Xu, Q. Huang, H. Ji, Y. Ge, Y. Yang, Q. Ren, S. Chen, Z. Jin and Y. Ding, *J. Environ. Chem. Eng.*, 2024, **12**, 113021.
67 Y. C. Hao, X. L. Dong, S. R. Zhai, X. Y. Wang, H. C. Ma and X. F. Zhang, *RSC Adv.*, 2016, **6**, 35709–35718.
68 V. D. Dang, J. Adorna Jr, T. Annadurai, T. A. N. Bui, H. L. Tran, L.-Y. Lin and R.-A. Doong, *Chem. Eng. J.*, 2021, **422**, 130103.
69 S. Li, S. Hu, W. Jiang, J. Zhang, K. Xu and Z. Wang, *J. Colloid Interface Sci.*, 2019, **556**, 335–344.
70 D. Ma, J. Wu, M. Gao, Y. Xin and C. Chai, *Chem. Eng. J.*, 2017, **316**, 461–470.
71 A. M. Bharathi, P. Mani, B. Neppolian, H. Sen Soo and T. Krishnamurthi, *J. Water Process. Eng.*, 2024, **58**, 104813.
72 F. Fu, H. Shen, W. Xue, Y. Zhen, R. A. Soomro, X. Yang, D. Wang, B. Xu and R. Chi, *J. Catal.*, 2019, **375**, 399–409.
73 H. Yang, J. Li, Q. Su, B. Wang, Z. Zhang, Y. Dai, Y. Li and L. a. Hou, *Chem. Eng. J.*, 2023, **470**, 144139.
74 J. Liu, L. Jiang, H. Zhang, H. Yao, J. Chai, J. Wang, D. Fang, Z. Zhang and M. Tie, *J. Alloys Compd.*, 2023, **956**, 170375.
75 Q. Xu, L. Zhang, B. Cheng, J. Fan and J. Yu, *Chem*, 2020, **6**, 1543–1559.
76 A. Shabbir, S. Sardar and A. Mumtaz, *J. Alloys Compd.*, 2024, **1003**, 175683.
77 S. Yao, F. Meng, H. Wei, W. Yu and H. Zhang, *J. Alloys Compd.*, 2024, **1005**, 176021.
78 R. Chen, W. Zhou, W. Qu, Y. Wang, L. Shi and S. Chen, *Appl. Surf. Sci.*, 2022, **588**, 152788.

79 Y. Zhen, C. Yang, H. Shen, W. Xue, C. Gu, J. Feng, Y. Zhang, F. Fu and Y. Liang, *Phys. Chem. Chem. Phys.*, 2020, **22**, 26278–26288.
80 W. Wang, W. Zhao, H. Huang, R. Chen and H. Shi, *Catal. Sci. Technol.*, 2021, **11**, 2948–2956.
81 M. Wang, M. You, P. Guo, H. Tang, C. Lv, Y. Zhang, T. Zhu and J. Han, *J. Alloys Compd.*, 2017, **728**, 739–746.
82 P. Guo, X. Hu and M. Wang, *Optik*, 2020, **222**, 165399.
83 J. Xu, Y. Liu and M. Chen, *Surf. Interfaces*, 2021, **25**, 101246.
84 A. A. Alemi, R. Kashfi and B. Shabani, *J. Mol. Catal. A:Chem.*, 2014, **392**, 290–298.
85 Z. Dai, F. Qin, H. P. Zhao, J. Ding, Y. L. Liu and R. Chen, *ACS Catal.*, 2016, **6**, 3180–3192.
86 Z. Liu, X. Q. Liu, C. L. Yu, L. F. Wei and H. B. Ji, *Sep. Purif. Technol.*, 2020, **247**, 116951.
87 N. Chen, M. Hu, L. Gou, L. Tan, D. Zhao and H. Feng, *Bull. Chem. Soc. Jpn.*, 2024, **97**, uoae030.
88 Q. Wu, Q. Zhang, W. P. Li, L. H. Luo and P. Du, *Chem. Eng. J.*, 2023, **475**, 146192.
89 H. F. Cheng, B. B. Huang and Y. Dai, *Nanoscale*, 2014, **6**, 2009–2026.
90 L. W. Zhang, T. G. Xu, X. Zhao and Y. F. Zhu, *Appl. Catal., B*, 2010, **98**, 138–146.
91 B. Zhu, H. Cheng, J. Ma, Y. Qin, Y. Kong and S. Komarneni, *Mater. Lett.*, 2020, **261**, 127099.
92 L. Cheng, D. Huang, Y. Zhang and Y. Wu, *Adv. Powder Technol.*, 2021, **32**, 3346–3354.
93 S. Dong, X. Liu, G. Tian, Y. Wang, G. Jin, Y. Zhao, J. Sun and M. Fan, *J. Alloys Compd.*, 2022, **892**, 162217.
94 M. Berradi, R. Hsissou, M. Khudhair, M. Assouag, O. Cherkaoui, A. El Bachiri and A. El Harfi, *Heliyon*, 2019, **5**, e02711.
95 T. Zhou, D. Xu, M. Lu, P. Wang and J. Zhu, *Res. Chem. Intermed.*, 2018, **44**, 6431–6444.
96 H. Cui, S. Dong, K. Wang, M. Luan and T. Huang, *Sep. Purif. Technol.*, 2021, **255**, 117758.
97 M. Govinda Raj, E. Vijayakumar, B. Neppolian, S. K. Lakhera and A. J. Bosco, *RSC Adv.*, 2021, **11**, 25511–25523.
98 A. Waehayee, S. Wangngae, J. Rungruengkit, T. Lerdwiriyanupap, T. Choklap, J. Prachanat, N. Pornnongsan, A. Ruangvittayanon, H. Nakajima, T. Chankhanittha, T. Butburee, S. Prayoonpokarach, A. Kamkaew, S. Suthirakun and T. Siritanon, *ACS Appl. Nano Mater.*, 2024, **7**, 6079–6092.
99 C. L. Yu, Z. Wu, R. Y. Liu, D. D. Dionysiou, K. Yang, C. Y. Wang and H. Liu, *Appl. Catal., B*, 2017, **209**, 1–11.
100 Q. Wang, Y. Zhao, Z. Zhang, S. Liao, Y. Deng, X. Wang, Q. Ye and K. Wang, *J. Mol. Liq.*, 2023, **383**, 122164.
101 S. Pramila, V. L. Ranganatha, G. Nagaraju and C. Mallikarjunaswamy, *Ionics*, 2024, **30**, 2901–2913.
102 Z. Wang, J. Li, S. Fu, D. Guo, J. Tang, X. Yang, R. Xu, G. Sui and S. Chen, *J. Solid State Chem.*, 2023, **322**, 123957.
103 G. Ren, J. Zhang, S. Li, L. Zhang, C. Shao, X. Wang and H. Bai, *Environ. Res.*, 2024, **252**, 118886.
104 R. Zhang, M. Xu, J. Yu, Z. Chen, J. Jiang, J. He and J. Hao, *J. Solid State Chem.*, 2023, **328**, 124330.
105 K. Li, M. Chen, L. Chen, S. Zhao, W. Xue and Y. Han, *Processes*, 2023, **11**, 1059.
106 S. C. Zhang, X. L. Li, M. Y. Huang, M. D. Shan, J. Chen, F. Q. Hao, J. M. Li, J. F. Luan, W. Zhang and F. B. Liang, *Chemistryselect*, 2022, **7**, e202200969.
107 N. L. Chen, M. Y. Hu, L. L. Gou, L. Tan, D. Zhao and H. X. Feng, *Bull. Chem. Soc. Jpn.*, 2024, **97**, uoae030.
108 L. Xue, J. Zhang, M. Sun, H. Zhang, K. Wang, D. Wang and R. Zhang, *Nanomaterials*, 2025, **15**, 834.
109 P. S. Nandisha, S. Yallappa, S. Joseph, B. Umesha, K. L. Nagashree and H. H. A. El-Gawad, *J. Cluster Sci.*, 2025, **36**, 109.
110 L. Ai, M. Zhao, L. Feng, L. Wang, D. Jia, N. Guo, C. Tan and M. Zha, *J. Alloys Compd.*, 2025, **1024**, 180189.
111 B. Zhao, Y. Xing, Y. Xue, N. Chen, C. Sun, M. Li, H. Shi, B. Ma, S. Wang, Y. Tang and J. Liu, *Chem. Eng. J.*, 2025, **511**, 161852.
112 T. Chankhanittha, B. Johnson, R. J. Bushby, T. Butburee, P. Khemthong and S. Nanan, *J. Alloys Compd.*, 2024, **1008**, 176764.
113 J. H. Yi, H. M. Mo, B. L. Zhang, J. X. Song, D. Q. Liu and G. J. Zhuo, *Sep. Purif. Technol.*, 2019, **211**, 474–480.
114 M. G. Jing, L. Chen, R. Li, C. M. Fan and Y. W. Wang, *Inorg. Chem. Commun.*, 2024, **162**, 112166.
115 L. R. H. Zhang, Q. H. Shen, L. X. Yu, F. L. Huang, C. T. Zhang, J. S. Sheng, F. Zhang, D. Cheng and H. Yang, *Crystengcomm*, 2020, **22**, 5481–5490.
116 F. S. Kang, G. D. Sheng, X. L. Yang and Y. Zhang, *Inorganics*, 2024, **12**, 289.
117 S. J. Li, C. J. You, F. Yang, G. J. Liang, C. Q. Zhuang and X. Li, *Chin. J. Catal.*, 2025, **68**, 259–271.
118 S. Zhou, X. Yu, J. Chen, L. Ma, F. Tao, J. Zhang, X. Zhao, T. Ren and H. Wang, *Sep. Purif. Technol.*, 2025, **372**, 133394.
119 S. Cao, L. Li, J. Dong, B. Wang, H. Wei, M. Ji, G. Liu, J. Xia and H. Li, *J. Alloys Compd.*, 2025, **1010**, 177807.
120 Y. Liu, L. Lu, A. Peyravi, Z. Hashisho, J. Zhao, X. Hao, J. Wang, H. Zhang, X. Chen, S. Zheng and Y. Tong, *Appl. Clay Sci.*, 2025, **273**, 107854.
121 Y. Li, H. Wang, J. Liu, X. Liu, J. Guan, J. Fu and S. Li, *Environ. Res.*, 2024, **263**, 120212.
122 Y. Xia, H. Liu, F. Sun, Z. Hao, B. Yue, X. Wang, Q. Ma, W. Yu, Y. Dong and X. Dong, *J. Environ. Chem. Eng.*, 2024, **12**, 114255.
123 J. Gu, M. Wu, L. Wang, F. Liu, S. He, M. Ding, Y. Yao, N. Tao, H. Sha, Z. Guo, H. Zhou, P. Zhou and P. Qiu, *J. Mol. Struct.*, 2025, **1343**, 142775.
124 Y. Jia, J. Shi, Z. Han, X. Liu, Y. Wang, Y. Song, Y.-G. Liu, R. Zhang, H. Zhang and H.-Y. Jiang, *Langmuir*, 2025, **41**, 13459–13467.
125 Z. Ma, J. Li, N. Wang, W. Guo and K. Zhang, *Molecules*, 2023, **28**, 6786.
126 Y. Wang, H. Zhu, P. He, M. Li, Y. Cao, Y. Du, Y. Wen, Y. Zhao, X. Liu and Y. Song, *Crystals*, 2025, **15**, 318.
127 M. Li, D. Li, Z. Zhou, P. Wang, X. Mi, Y. Xia, H. Wang, S. Zhan, Y. Li and L. Li, *Chem. Eng. J.*, 2020, **382**, 122762.
128 M. Tuerhong, P. Chen, Y. Ma, Y. Li, J. Li, C. Yan and B. Zhu, *J. Solid State Chem.*, 2022, **315**, 123468.

129 J. Liang, F. Liu, J. Deng, M. Li and M. Tong, *Water Res.*, 2017, **123**, 632–641.
130 Z. Li, X. Meng and Z. Zhang, *Catal. Today*, 2018, **315**, 67–78.
131 J. Liang, J. Deng, F. Liu, M. Li and M. Tong, *Colloids Surf., B*, 2018, **161**, 528–536.
132 H. Shi, J. Fan, Y. Zhao, X. Hu, X. Zhang and Z. Tang, *J. Hazard. Mater.*, 2020, **381**, 121006.
133 Y. Han, H. Zeng, H. Li, X. Niu, X. Liu, D. Zhang, H. Fan and K. Wang, *Surf. Interfaces*, 2025, **56**, 105685.
134 H. Yang, Z. Zhang, J. Li, L. Song and B. Wang, *Chem. Eng. J.*, 2024, **487**, 150554.
135 Z. Y. Ma, K. Cao, S. T. Gao, X. F. Chen and Y. Q. He, *J. Environ. Manage.*, 2025, **376**, 124561.
136 X. D. Liu, R. Y. Chen, Y. Q. Pi, J. H. Sun, C. F. Yu, J. H. Li and S. Y. Dong, *Sep. Purif. Technol.*, 2025, **354**, 129265.
137 X. F. Shen, B. T. Song, X. X. Shen, C. Shen, S. D. Shan, Q. Q. Xue, X. B. Chen and S. J. Li, *Chem. Eng. J.*, 2022, **445**, 136703.
138 B. S. Li, C. Lai, M. M. Zhang, S. Y. Liu, H. Yi, X. G. Liu, N. An, X. R. Zhou, L. Li, Y. K. Fu, L. Qin and L. Chen, *Chem. Eng. J.*, 2021, **409**, 128281.
139 P. Y. Hao, Z. Z. Chen, Y. J. Yan, W. L. Shi and F. Guo, *Sep. Purif. Technol.*, 2024, **330**, 125302.
140 M. Shi, H. Y. Yang, Z. H. Zhao, G. M. Ren and X. C. Meng, *Chem. Commun.*, 2023, **59**, 4274–4287.
141 K. L. Zhang, X. D. Sun, H. T. Wang, Y. L. Ma, H. W. Huang and T. Y. Ma, *Nano Energy*, 2024, **121**, 109206.
142 H. B. Zhou, K. L. Wu, X. W. Luo, Q. H. Cai, J. Zeng, Y. Z. He, X. Y. Liu, S. Q. Li and S. P. Wei, *J. Colloid Interface Sci.*, 2025, **677**, 827–841.
143 K. Thamaraiselvi, G. Palanisamy, P. S. M. Kumar, J. Lee and J. J. Shim, *Chem. Eng. J.*, 2025, **511**, 161947.
144 E. Fekri, M. S. S. Dorraji and M. Vahedpour, *Sol. Energy Mater. Sol. Cells*, 2025, **281**, 113315.
145 K. Zhong, P. P. Sun and H. Xu, *Small*, 2025, **21**, 2310677.
146 D. Suri, S. Das, S. Choudhary, G. Venkanna, B. Sharma, M. A. Afroz, N. K. Tailor, R. Joshi, S. Satapathi and K. Tripathi, *Small*, 2025, **21**, 2408981.
147 B. Rhimi, M. Zhou, Z. X. Yan, X. Y. Cai and Z. F. Jiang, *Nano-Micro Lett.*, 2024, **16**, 64.
148 B. Yu, Y. X. Wu, F. M. Meng, Q. Wang, X. Q. Jia, M. W. Khan, C. M. Huang, S. Y. Zhang, L. Yang and H. Wu, *Chem. Eng. J.*, 2022, **429**, 132456.
149 Z. L. Wang, B. Cheng, L. Y. Zhang, J. G. Yu, Y. J. Li, S. Wageh and A. A. Al-Ghamdi, *Chin. J. Catal.*, 2022, **43**, 1657–1666.
150 Q. Jiao, B. C. Gao, L. Zhang, R. J. Chen, L. Wang, Q. Wang, N. J. Feng, H. Wan, G. F. Guan and M. J. Han, *Colloids Surf., A*, 2025, **726**, 137798.
151 A. N. Singh, R. Anand, M. Zafari, M. Ha and K. S. Kim, *Adv. Energy Mater.*, 2024, **14**, 2304106.
152 H. Q. Wang, Z. H. Chen, Y. R. Shang, C. D. Lv, X. H. Zhang, F. Li, Q. Z. Huang, X. D. Liu, W. M. Liu, L. Zhao, L. Q. Ye, H. Q. Xie and X. L. Jin, *ACS Catal.*, 2024, **14**, 5779–5787.
153 R. J. Wu, S. Gao, C. Jones, M. M. Sun, M. Guo, R. Tai, S. W. Chen and Q. Wang, *Adv. Funct. Mater.*, 2024, **34**, 2314051.
154 Q. B. Dong, X. M. Li, J. H. Sun, Y. Y. Zhu, X. X. Liang, H. T. Ren, A. Labidi, D. Wang, F. Li and C. Y. Wang, *J. Catal.*, 2024, **433**, 115489.
155 Z. Y. Liu, M. Luo, Y. Cao, L. H. Meng, Y. Yang and X. M. Li, *J. Catal.*, 2024, **430**, 115347.